Division
SE Solar Energy Research

The solar energy division of the HMI concentrates its research activities on the exploration of the potential of highly productive thin-film technologies for solar cells of „tomorrow“ and „beyond“. The main objective is to realize systems which lead to substantial cost reduction at high conversion efficiency. This requires research for improvements of materials and systems which are already at the edge of being industrialized but also research for new materials and innovative solar cell structures. Therefore, the activities reach from basic material research to the development of technologies for solar cells and minimodules on the laboratory scale.

The work is supported by the broad range of analytical methods available in both sections of the HMI, particularly in the field of surface and interface physics, defect spectroscopy, ion-beam techniques and structural characterization, solid states physics, as well as conventional material and device analysis.

The groups collaborate in numerous projects and networks with national and international partners. The division Solar Energy Research comprises 5 scientific departments:

SE1 Silicon Photovoltaics
SE2 Heterogeneous Material Systems
SE3 Technology
SE4 Dynamics and Interfacial Reactions
SE5 Solar Energetics

and the group

SE6 Electronic Structure of Semiconductor Interfaces

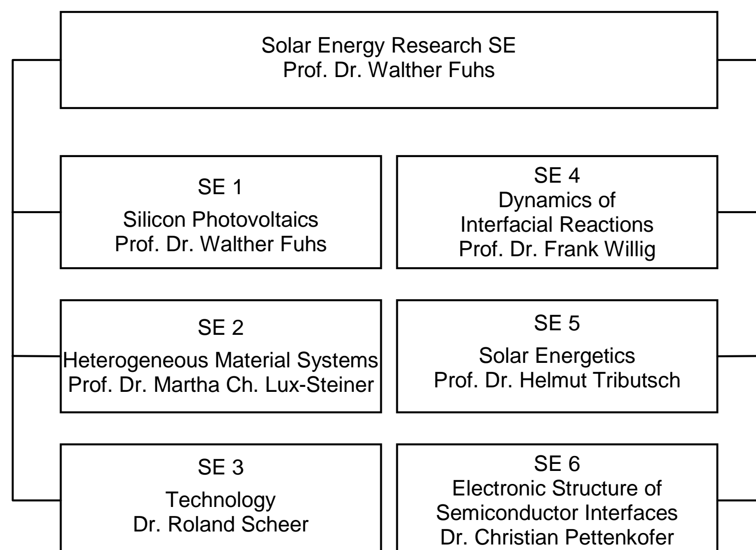

Aluminium-induced layer exchange – Influence of the oxide layer

A future generation of silicon thin-film solar cells could well be based on polycrystalline silicon (poly-Si) on foreign substrates with grain sizes larger than the thickness of the active Si layers. A promising approach for such a development is the formation of a thin large-grained poly-Si seed layer on a glass substrate and a subsequent homoepitaxial thickening of this seed layer by a low-temperature deposition process ($T \leq 600°C$). A very attractive process for seed layer formation is the aluminium-induced layer exchange (ALILE) which makes use of aluminium-induced crystallisation of amorphous silicon (a-Si). In this process an initial film sequence glass/Al/a-Si is transformed into a glass/poly-Si/Al+Si film stack. The transformation takes place during an annealing step at temperatures well below the eutectic temperature of the Al/Si system (T_{eu} = 577°C). The process starts with the local formation of Si nuclei within the Al layer. These Si nuclei grow in lateral direction until adjacent Si grains touch each other and finally form a continuous poly-Si film on the glass substrate [1,2].

So far the mechanism of crystallisation in the ALILE process is only poorly understood. It has been speculated that a thin oxide layer is essential for the process between the initial Al and the initial a-Si layer which may be formed by oxidation of the initial Al layer during the vacuum break prior to the a-Si layer deposition. We have addressed this question using energy-filtered TEM and electron energy loss spectroscopy to analyse the distribution of Al, O and Si at the Al/a-Si interface. These studies proved convincingly that an Al-oxide layer had formed during the vacuum break. For a more quantitative understanding we studied the growth of the poly-Si films for samples where an oxide layer had been grown deliberately by exposing the Al film for different oxidation times t_{OX} to an atmosphere with a partial pressure of oxygen of $6.5 \cdot 10^{-3}$ mbar. The poly-Si film growth can be observed during the annealing process by placing the sample in a heat stage of an optical microscope and observing the reflection from the initial glass/Al interface through the glass substrate.

Fig. 1 shows the crystallised fraction (ratio of poly-Si area to total area) as a function of the annealing time at a temperature of 420 °C for different oxidation times. The thinner the oxide layer, the faster is the layer exchange. However, this enhancement of crystallisation for thin oxide layers is connected with a strong increase of the number of Si grains (Fig. 2, blue curve) which results in a reduction of the average grain size. The average area of a single grain equals the total area under investigation divided by the number of grains. Assuming a square shape for the grains, we calculated the edge length of the squares and defined this as the estimated grain size. With increasing thickness of the oxide the number of nuclei decreases and the average grain size increases correspondingly (Fig.2).

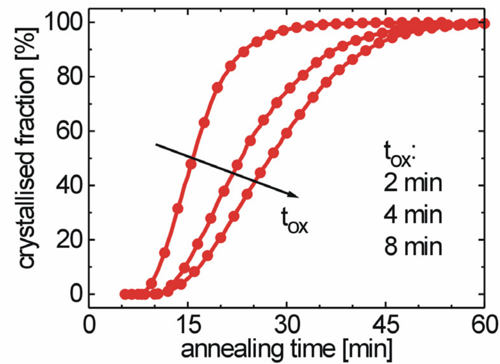

Fig. 1: Crystallised fraction versus annealing time for different oxidation times t_{ox}.

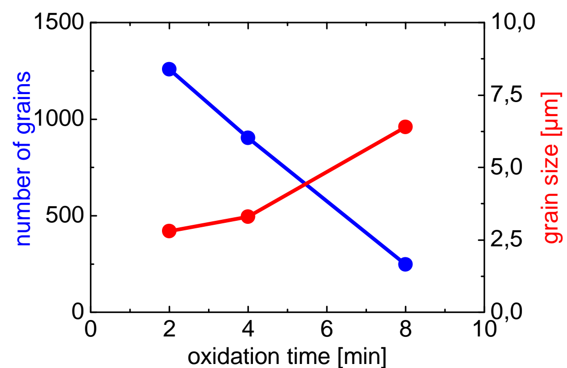

Fig. 2: Number of grains (blue curve) within the area under investigation (A = 100µm x 100µm) and the resulting estimated grain size (red curve) versus oxidation time.

These results underline the important role of the oxide layer for nucleation and growth of the poly-Si film. The working hypothesis is that the oxide layer acts as a barrier for the diffusion of Si (Al) into the initial Al layer (a-Si layer). The thicker the oxide layer, the lower is the number of grains and the longer is the process time to complete the layer exchange process. In this view nucleation is related inhomogeneities or defects in the thin oxide layer. This experience opens new process paths for actively controlling the nucleation rate.

[1] S. Gall, J. Schneider, M. Muske, I. Sieber, O. Nast, W. Fuhs, Proceedings of PV in Europe (2002), in press.
[2] I. Sieber, R. Schneider, I. Doerfel, P. Schubert-Bischoff, S. Gall, W. Fuhs, Thin Solid Films (2003), in press

S. Gall, J. Schneider, M. Muske, I. Sieber, W. Fuhs

Amorphous/crystalline-silicon heterojunction solar cells

Heterojunctions between hydrogenated amorphous silicon, a-Si:H, and crystalline silicon, c-Si, can be made at low process temperatures of typically 150-200 °C and therefore offer a low-temperature and low-cost alternative to the traditional silicon wafer technology. The so far best results have been obtained by Sanyo Corporation. Using textured n-type silicon wafers Sanyo reached an efficiency of 20.7 % for a laboratory cell where for both the emitter and the back contact a-Si:H technology was employed. The focus of our work is to develop this low-temperature technology for application in case of temperature sensitive silicon absorbers such as poly-Si films but also multicrystalline or band-grown Si-material. Since these absorbers are in general p-type we so far have worked with heterojunctions on p-type Si wafers only. The best result which we obtained in close collaboration with the FU Hagen in the frame of a networking project (BMBF) is illustrated in Fig.1.

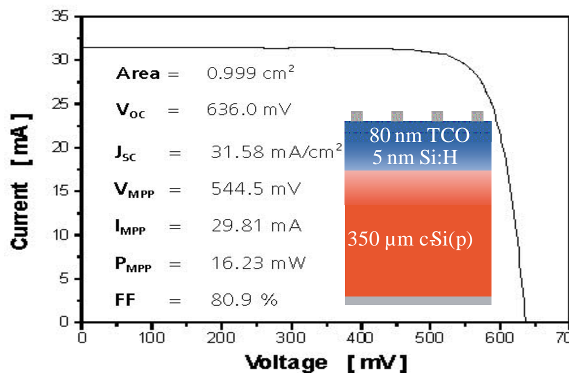

Fig. 1 I-U characteristics of an a-Si:H(n)/c-Si(p) solar cell (certified by ISE-Freiburg). Inset shows a schematic sketch of the structure.

The structure is TCO/a-Si:H(n$^+$)/c-Si(p) with back surface field (BSF). The transparent conducting oxide, TCO, was indium tin oxide (ITO) but similar results have also been obtained using ZnO:Al as window material. This solar cell with an area of 1 cm^2 has a certified efficiency of 16.23 %. This is to our knowledge the best result so far published for this inverse structure on a p-type flat Si wafer.

The most critical part in this cell structure is the preparation and optimization of the a-Si:H emitter. In order to develop a deeper understanding of the physics of this device we carefully analysed bulk and interface properties of such amorphous layers and studyied the cell parameters as a function of the thickness d. The result is that the optimum emitter thickness is close to d = 5 nm. At higher values of d the optical absorption in the emitter becomes a limiting factor and at lower values there is a detrimental influence of the TCO work function and of emitter shorts on the a-Si:H/c-Si heterojunction. It turned out that the properties of the above solar cells were not limited by the quality of the hetero-interface. This results from the fact that the active heterointerface is perfectly passivated by an optimized wafer precleaning and an a-Si:H(n) layer deposition process. For this purpose special analytical tools including such for getting information on an atomic depth scale were developed.

The amorphous films were deposited by plasma enhanced chemical vapor deposition (PECVD) from gas mixtures of silane SiH_4 and phosphine PH_3 at a substrate temperature of 170 °C. UV-excited constant final state yield spectroscopy (CFSYS) is used to study the density of states distribution in such films. Comparison with results from photoyield measurements proved that this method has advantages as compared with UPS and gives the most reliable results.

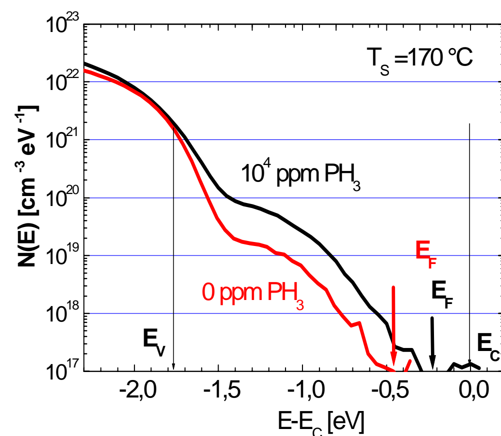

Fig.2 Density of state distribution resulting from CFSYS measurements of a doped (10000 ppm PH_3 /SiH_4) and a non doped ultrathin a-Si:H(n) films on crystalline silicon. Deposition temperature was 170 C.

Fig. 2 compares the gap state distributions and Fermi level positions of undoped and phosphorus doped films. Doping clearly leads to a shift of the Fermi level towards the conduction band from E_C – E = 0.5 eV to 0.25 eV. This is connected with a pronounced increase of the concentration of deep gap states and a flattening out of the band tail at the valence band. Qualitatively these observations are similar as in case of thick amorphous films. However, there are pronounced quantitative differences in particular in case of undoped a-Si:H which for thick films would have much lower N(E) values.

Fig. 3 shows that the doping effect saturates at a gas phase doping level of about 10^4 ppm. For the performance of the solar cell the Fermi level position in the thin film is a crucial parameter. The Fermi level position determines the minimal emitter layer thickness which allows to screen the field penetration from the TCO-a-Si:H(n) contact and thus the reachable band bending in the absorber. The Fermi level position here amounts to about E_C-E_F = 0.25 eV. Of course this value strongly depends on the deposition and posttreatment conditions. This is the first investigation of the behavior of ultra thin a-Si:H emitter films on c-Si substrates by CFSYS.

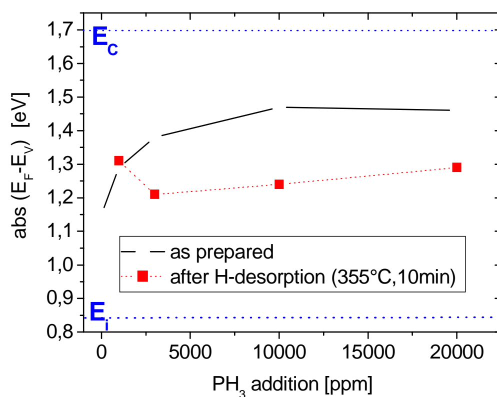

Fig. 3 Position of the Fermi level in a-Si:H films with different doping levels before and after H-desorption.

The dependence of the cell parameters on the thickness d of the emitter layer is presented in Fig. 4. These results reflect the opposing influence of two effects which leads to optimum performance at a value of around 5 nm. The short circuit current j_{SC} decreases continuously with increasing d due to the increase of optical absorption in the a-Si:H(n^+) layer and their extreme low contribution to the photocurrent if the a-Si:H emitter layer becomes thicker (dead layer). The second opposing influence consists in the decrease of the open circuit voltage V_{OC}. Two explanations may be given to this behavior. The break down of V_{OC} may be the result of imperfections (shunts) in the ultra-thin a-Si:H film. However, measurements of surface photovoltage (SPV) suggest as an alternative explanation that the band bending in the Si-wafer is reduced at very low thicknesses. The TCO-layer may form a Schottky contact with the a-Si:H(n^+) the field of which penetrates into the c-Si space charge region thus reducing V_{OC}. Such results suggest that the TCO is not just acting as a window material but also influences the electronic structure of the heterojunction. Therefore the complete contact system TCO/a-Si:H/c-Si has to be analysed and considered in a process of optimisation.

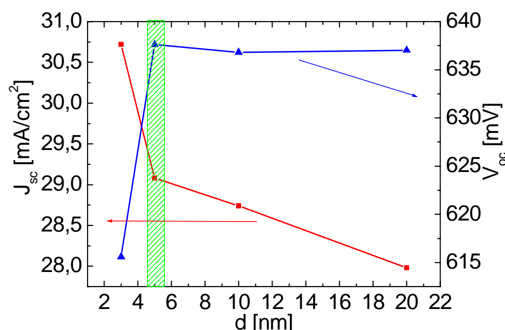

Fig. 4. Experimental determined parameters J_{sc} and V_{oc} of the TCO/a-Si:H(n) /c-Si(p) solar cell in dependence on the a-Si:H(n) emitter thickness.

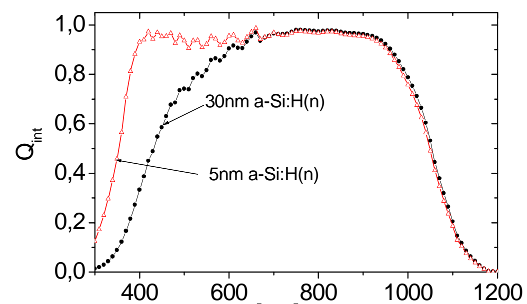

Fig. 5.Internal Quantum efficiency of a-Si:H(n)/c-Si(p) solar cell with 5 nm and 30 nm emitter, respectively.

Fig. 5 shows that in fact the internal quantum efficiency in the short wavelength region is strongly enhanced when the thickness descreases from 30 nm to 5 nm. The blue response in the case of a 5 nm thick emitter layer is limited by the TCO absorption edge.

Thes results make evident that the whole TCO/a-Si:H/c-Si system has to be analyzed and considered for an optimization of the solar cell device.

A detailed analysis of the temperature dependence of V_{OC} and the dark saturation current of the hetero solarcell presented in Fig. 1 and Fig. 5 shows that the cell efficiency is not limited by the a-Si:H(n)/c-Si(p) interface, but by the quality of the absorber and the rear contact. Therefore further improvements are possible by an optimisation of the back contact and the absorber. In addition the use of light trapping structures will increase J_{SC} and will not reduce V_{OC} as long as the interface of the heterojunction is well passivated.
Results are published in Ref.1-4

[1] M.L.D. Scherff, A. Froitzheim, A. Uljaschin, M. Schmidt, W.R. Fahrner, W. Fuhs, Proceedings of PV in Europe (Rome, Oct. 2002), in press
[2] M. Schmidt, A. Froitzheim, R. Stangl, L. Elstner, K. Kliefoth, W. Fuhs, Proc. of 17th Europ. Photovoltaic Solar Energy Conf. (2001), 1383
[3] M.Schmidt, O. Milch, Th.Lußky, A.Schöpke, Mat. Res. Soc. Symp. Proc. (San Francisco, 2003), accepted.
[4] A.Froitzheim, R.Stangl, L.Elstner, W.Fuhs, 29th IEEE Photovoltaic Solar Energy Conf. (New Orleans, Mai 2002).

A. Froitzheim, R. Stangl, H. Angermann, L. Elstner, W. Fuhs, K. Kliefoth, A. Laades, A. Schöpke, M. Schmidt

Laser crystallisation of amorphous silicon: texture-formation on metals

Excimer laser crystallization of hydrogenated amorphous silicon (*a*-Si:H) is a well-established method to produce polycrystalline silicon (poly-Si) with a grain size of up to 5µm. The goal is to use laser-crystallized poly-Si as a seed layer for an epitactically grown absorber. Due to the short absorption depth of poly-Si, a back contact and a reflector are necessary for solar cell applications. In addition to the electrical back-contact, a thin metal layer on the glass substrate can be utilized as the reflector. For this purpose, we developed for the first time a reliable process for laser-crystallization of *a*-Si:H on molybdenum (Mo) coated glass.

Undoped *a*-Si:H films were deposited at 230 °C by plasma-enhanced chemical vapor deposition (PECVD) on Mo coated glass substrates to a thickness of ≈ 80 nm. The thickness of the Mo layer varied between 100 and 200 nm. The *a*-Si:H films were crystallized using a XeCl excimer laser (wavelength 308 nm, pulse duration ≈ 20 ns). To prevent explosive out-diffusion of hydrogen the specimens were crystallized using a step-by-step crystallization procedure. In Fig. 1 the average grain size, <*x*>, of the laser-crystallized poly-Si determined from SEM images is plotted as a function of the final laser fluence, E_L, for a Mo layer thickness of 100 and 200 nm. The samples containing a 100 nm thick Mo layer show the same crystallization regimes that are well known from the crystallization of poly-Si on glass and quartz substrates. At small laser fluences ($E_L \leq 450$ mJ/cm^2) the *a*-Si:H layer is partially molten which results in the formation of small grained poly-Si (<*x*> ≈ 100 nm). At $E_L \geq 530$ mJ/cm^2 the *a*-Si:H film is completely molten which also results in the formation of small grained poly-Si since epitaxial re-growth from the substrate cannot occur. In between these two melting regimes a laser-fluence window exists where <*x*> increases to about 450 nm. This regime is called the super lateral growth (SLG). The dependence of the average grain size on E_L is similar to samples that do not contain a metal layer between substrate and poly-Si (open diamonds in Fig.1). However, the presence of the thin metal layer causes a significant reduction of <*x*> by about a factor of 4 compared to the crystallization of an a-Si:H layer with identical thickness on quartz. Additionally, E_{SLG} depends critically on the Mo layer thickness. A 200 nm thick Mo layer results in an increase of E_{SLG} to about 770 mJ/cm^2. The shift of E_{SLG} to 770 mJ/cm^2 is accompanied by a pronounced increase of the maximum average grain size to 900 nm. This might be due to a change of the heat diffusion through the metal-substrate structure [1].

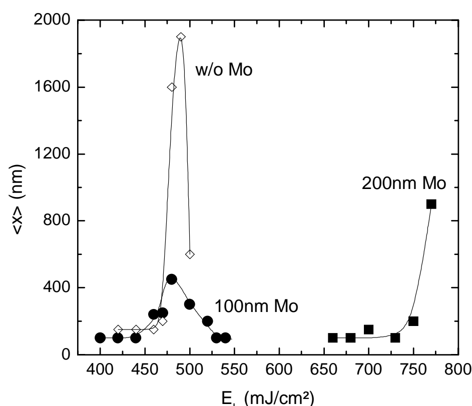

Fig. 1: Average grain size, <*x*>, of poly-Si as a function of the laser fluence, E_L, for Mo layers with a thickness of 100 nm (circles), 200 nm (squares) and without a Mo layer (open diamonds). The thickness of the *a*-Si:H layer is 80 nm. The lines are guides to the eye.

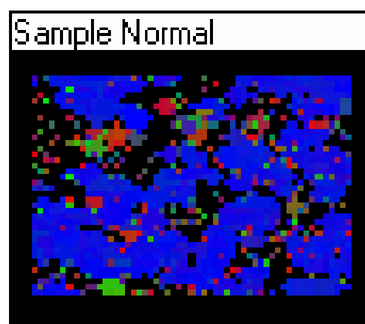

Fig.2: Orientation mapping from electron backscattering diffraction measurements. Red, green, and blue represent (100), (110), and (111) oriented grains.

The results shown above reveal that the crystallization process is not influenced by a thin Mo layer. This is further corroborated by the fact that on Mo coated glass a preferential {111} orientation in the direction of the surface normal is observed for specimens crystallized in the SLG regime. Recently, the same observation was reported for poly-Si on quartz. Fig. 2 shows results of grain orientation measurements from electron backscattering diffraction. The specimens exhibit a pronounced preferential {111} orientation of the silicon grains. Other metals investigated such as Al resulted in significant damage of the silicon layer during laser crystallization [2].

K. Brendel, N. H. Nickel, P. Lengsfeld, W. Fuhs

[1] K. Brendel, P. Lengsfeld, I. Sieber, A. Schöpke, M. Nerding, H. P. Strunk, N. H. Nickel, and W. Fuhs, J. Appl. Phys. **91**, 2969 (2002).
[2] K. Brendel, P. Lengsfeld, I. Sieber, A. Schöpke, M. Nerding, H. P. Strunk, N. H. Nickel, and W. Fuhs, Thin solid films, at press (2003)

Recombination in $Cu(In, Ga)S_2$ thin-film solar cells

As we have shown in our previous work, recombination via interface states at the $CuInS_2$/CdS interface dominates the transport of charge carriers in $CuInS_2$ solar cells. This explains the open circuit voltages of about 750 mV which is a moderate value in view of the absorber band gap E_g of 1.5 eV. In this study we investigate the influence of the incorporation of Ga into the chalcopyrite absorber on the dominating transport mechanism. Recom-bination losses are analyzed by measuring *j(V)* curves as a function of temperature and illumination.

The activation energy of the dominating recombination is determined from the slope of an Arrhenius plot of the saturation current density which is corrected for the temperature dependence of the diode quality factor. As shown in Fig. 1, the $CuInS_2$ cells show activation energies below the absorber band gap, due to the dominating recombination at the interface over a barrier which is reduced by the unfavourable band line-up or Fermi-level pinning at the $CuInS_2$/CdS interface. In contrast, the investigated $Cu(In,Ga)S_2$ cell shows an activation energy equivalent to the absorber band gap, indicating that recombination in the space charge region dominates the current transport.

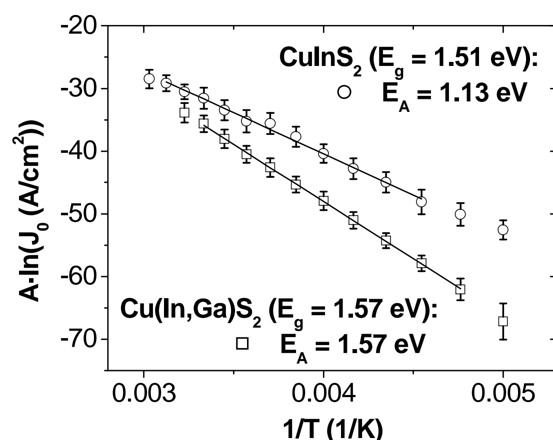

Fig. 1: Corrected saturation currents for $Cu(In,Ga)S_2$ cells depending on absorber composition

Proportional to the increase of the activation energy one could theoretically expect an increase of the open circuit voltage. But so far, the highest observed open circuit voltages correspond only to an increase of about 40 mV beyond the increase in the band gap. We can explain this behavior by the stronger influence of tunneling assistance to the recombination which we observe for the cells with higher activation energies. Therefore the increase in activation energy due to shifting the dominating recombination from the interface into the absorber cannot yet be fully converted into an increase of the open circuit voltage. To this aim the tunneling has to be reduced by proper device design.

To explain the described changes in the recombination mechanism we presume that positive interface charge determines the band bending towards the absorber/buffer interface as well as towards absorber grain boundaries. In this we follow the assumption that intergrain interfaces in the polycrystalline absorber layer have interface states of the same type as the $CuInS_2$/CdS interface states, as it was postulated to explain the oxygenation and air annealing effects on the electronic properties of $Cu(In,Ga)Se_2$ devices [1].

In case of dominating interface recombination the activation energy of the saturation current is a measure of the band bending towards the interface. The band bending towards the grain boundaries can be deduced from the temperature dependence of the series resistance. The temperature dependence of the series resistance of cells with a typical non-oriented grains structure is shown in Fig. 2. The series resistance increases with decreasing temperature with an activation energy which we can ascribe to the height of the potential barriers at the grain boundaries in the absorber. For comparison, the temperature dependence of the series resistance is shown for a cell with a columnar grain structure. Due to the lack of grain boundaries in the transport direction of the diode current, these particular cells don't show increasing but decreasing series resistance with decreasing temperature.

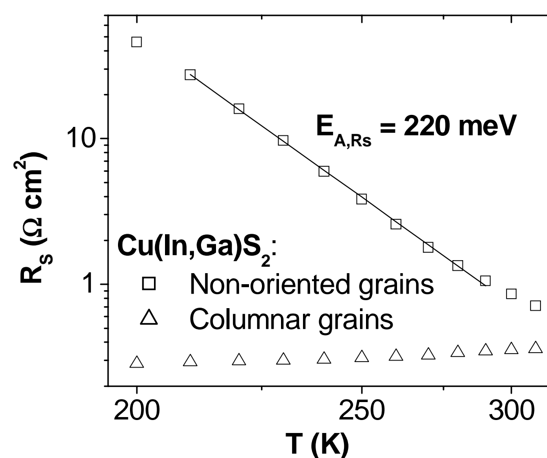

Fig. 2: Temperature dependence of the series resistance for $Cu(In,Ga)S_2$ cells depending on absorber grain structure

Analysis of a large number of cells reveals that the activation energy of the series resistance as well as the activation energy of the saturation current are varying with absorber composition and illumination. There are, however, strongly correlated. While there are a number of mechanisms which could in principle shift the dominant recombination away from the heterointerface, this correlation confirms the original assumption. Hence, it has to be concluded that the incorporation of Ga increases interface charges, thereby increasing the band bending to a value that prevents excessive recombination at the absorber heterointerface.

Reference
[1] U. Rau, J. Appl. Phys. 86 (1999) 497

J. Reiß, S. Bakehe, R. Klenk, M.C. Lux-Steiner

Chalcopyrite Thin Film Tandem Cell with V_{OC} = 1.2V

A stacked tandem cell based on a $Cu(In,Ga)Se_2$ bottom and a $CuGaSe_2$ top cell is prepared. The efficiency of the complete cell is 7.4% with an open circuit voltage of 1.18V.

One main objective to investigate and develop wide gap chalcopyrite solar cells is the ultimate goal of a thin film tandem solar cell, using the well developed $Cu(In,Ga)Se_2$ absorber for the bottom cell, utilizing the "red" part of the solar spectrum, and a wide gap chalcopyrite, e.g. $CuGaSe_2$ for the top cell, to harvest the "blue" light. Taking the solar spectrum into account one can estimate a factor of 1.5 improvement for the efficiency compared to a pure $Cu(In,Ga)Se_2$ cell. Therefore a cell with 30% efficiency seems feasible, combining high efficiency with the economic advantages of thin film solar cells. Before a commercial tandem cell will be within reach a number of problems are still to be solved. The ultimate goal is a monolithic tandem cell with the top cell prepared directly on top of the bottom cell, but as an intermediate step we develop stacked tandem cells with separate $Cu(In,Ga)Se_2$ and $CuGaSe_2$ cells on their individual substrate glasses. The four terminal device is wired in series (as would be a monolithic tandem cell).

The bottom cell is a standard $Cu(In,Ga)Se_2$ cell with an absorber from the Shell Solar pilot line, and the CdS-buffer, ZnO window and NiAl grid prepared by the HMI base line. The top cell is a transparent $CuGaSe_2$ cell based on ITO as a transparent back contact with a $CuGaSe_2$ absorber layer prepared in our standard two stage process, CdS buffer, ZnO window and NiAl grid. A thin Au-wire is soldered to the front grid of the $Cu(In,Ga)Se_2$ solar cell and to the ITO back contact of the $CuGaSe_2$ top cell to connect the two cells in series. IV curves are measured in our solar simulator. Optical transmission is measured in a UV-VIS spectrometer.

I - V curves in the dark and under illumination of the $CuGaSe_2$ cell show no indication of a counter diode at the back contact. This counter diode would be expected taking the band alignment and the doping of the $CuGaSe_2$ and the ITO into account. Currently we have no understanding why this contact behaves ohmic. But this phenomenon has been observed by others too, therefore the ITO back contact appears as a feasible way to prepare transparent top cell. Fig. 1 shows the IV curves under illumination of the individual cells and the tandem cell. The $Cu(In,Ga)Se_2$ cell is measured as illuminated through the transparent $CuGaSe_2$ cell. As becomes clear the current is limited by the current through the bottom cell which naturally shows a reduced current compared to illumination by the full solar spectrum. Still, this current is much less than one would expect

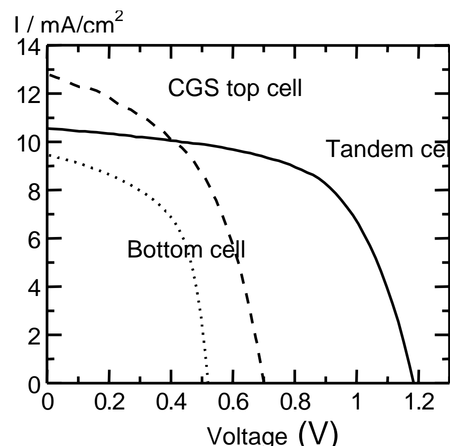

Fig. 1: J-V characteristics of the individual cells and the tandem cell

from the solar spectrum transmitted through $CuGaSe_2$ with a band gap of 1.7 eV.

Therefore transmittance measurements have been performed on untreated ITO films, $CuGaSe_2$ on glass and on the $CuGaSe_2$ on ITO solar cell. The results show clearly that the ITO lost transparency due to the $CuGaSe_2$ deposition process. It is likely that a reaction with Se at the high deposition temperatures leads to the reduced transparency of the ITO. Future work will focus on the reason for the transparency loss and on ways to keep the ITO transparent throughout the deposition process.

Nevertheless a tandem cell with the parameters given in table I has been obtained. Certainly the efficiency is not remarkable especially since it is lower than the efficiency of the original $Cu(In,Ga)Se_2$ solar cell when illuminated with the full solar spectrum. But the open circuit voltage of almost 1.2V is remarkable and the work shows that a first step towards stacked tandem cells has been taken.

Table I: PV parameters of the tandem cell

V_{OC}/V	1.18
j/mA/cm^2	10.6
FF/%	60
η/%	7.4

Reference

[1] S. Nishiwaki, S. Siebentritt, P. Walk, M. C. Lux-Steiner, Prog. in Photovoltaics 11 (2003) 1-6

S. Siebentritt, S. Nishiwaki, P. Walk

$CuGaSe_2$ thin films prepared by a novel Chemical Close-Spaced Vapor Transport (CCSVT) technique for photovoltaic application

The novel CCSVT-technique

Sustaining excellent photovoltaic material properties at reduced deposition temperature and high deposition rates represents an unique challenge for further process development.

Very recently, a halogen-supported chemical vapor transport technique (CCSVT) has been highly successfully implemented allowing fast and large-area deposition of high quality semiconducting chalcopyrite thin films for photovoltaics. A schematic drawing of the system is shown in Fig. 1 (for details see Ref. 1).

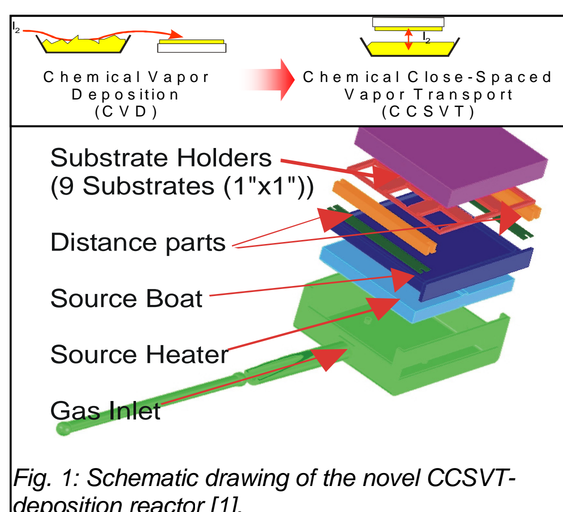

Fig. 1: Schematic drawing of the novel CCSVT-deposition reactor [1].

First results

Thin metallic Cu films deposited on clean and Mo-coated soda lime glass (SLG) substrates are thermally and chemically treated under gaseous $GaCl_x/H_2Se$ atmosphere in the CCSVT cell. The Ga_2Se_3 employed as source material is stoichiometrically volatilized by a controlled amount of HCl/H_2 agent at a certain pressure. The thin film deposition of Ga_2Se_3 binary source material was performed under varying conditions of the source temperature (T_{source}), the substrate temperature ($T_{substrat}$), the distance between source material and substrate holder ($D_{source-substrate}$), the reactor pressure ($p_{reactor}$) and the gaseous HCl content within H_2 carrier gas (Q_{HCl}/Q_{H2})

Single phase $CuGaSe_2$ layers are prepared with a growth rate of 230-240 nm/min by using a single stage process. A two stage process is applied for the fine tuning of the $CuGaSe_2$ composition and electronic properties appropriate for the solar cells preparation. Particularly, the Ga-to-Cu ratio is controlled within an error of 3.0% of the as-prepared films. The CCSVT-process parameters have been summarized and compared with conventional used evaporation process parameters in the table.

Parameters	CCSVT	evaporation
T(source) [°C]	520 - 580	1200–1400 (Cu/Ga) 300 (Se)
T(growth) [°C]	450 - 520	> 600
Growth rates [nm/min]	240	< 200
materials use [%]	50 - 60	5– 50 (Cu/Ga) ≤ 10 (Se)

Film characterization including X-ray diffraction (XRD) measurements, scanning electron microscopy (SEM) observations, transmission electron microscopy (TEM) studies, X-ray fluorescence analysis (XRF) and elastic recoil detection analysis (ERDA) has been carried out (see Fig.2). By means of the ERDA method, high depth homogeneity of the deposited $CuGaSe_2$ layers was observed. The detected Na distribution in the depth profile favors a back side field.

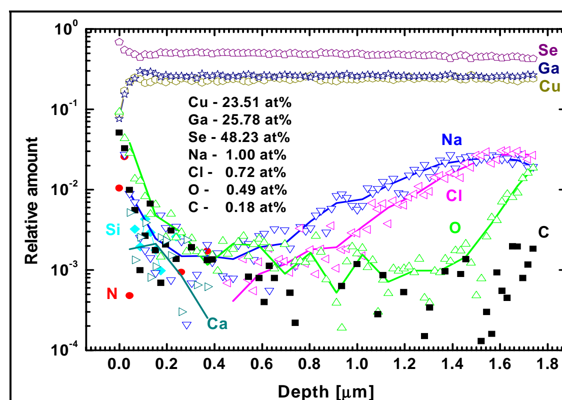

Fig. 2: Chemical composition of thin $CuGaSe_2$ film detected by elastic recoil detection analysis (ERDA).

The solar cell devices consisting of Mo/CGSe/CdS/ZnO heterostructures show under AM1.5 conditions a total area efficiency of maximal 7.0% with V_{oc} = 788 mV and J_{sc} = 15.19 mA/cm^2.

Reference

[1] Verfahren und Anordnung zum Abscheiden von Material aus einem Vorrat, DE 102 08 911.6 AT: 27.02.2002.

M. Rusu, S. Wiesner, S.M. Babu, D. Fuertes Marrón, K. Höhn, A. Jäger-Waldau, S. Lindner, A. Meeder, T. Münchenberg, A. Rumberg, Th. Schedel-Niedrig, R. Würz and M. Ch. Lux-Steiner
W. Bohne, W. Fritsch

ILGAR-ZnO/CIGSSe solar cells – effects of damp/heat exposure

The main goal of the project is the further progress in chemical low-cost methods for the deposition of semiconductor thin layers, mainly the ILGAR process (Ion Layer Gas Reaction, patents by HMI). The classical ILGAR is limited to a layer thickness of 100 nm due to the limited growth rate of involved dip steps. In order to deposit µm-layers an ILGAR spray process has been developed. Thin film solar cells with so-prepared CIGS ($Cu(In,Ga)S_2$) absorbers have already reached an efficiency of 3.5%.

Effects of damp/heat (DH) exposure on ZnO-WEL/CIGSSe solar cells (WEL=Window Extension Layer, CIGSSe=$Cu(In,Ga)(S,Se)_2$)

ZnO WELs (i.e., buffer layers of the same material as the sputtered window, but deposited by a mild process) were optimized such that record efficiencies up to η=15% could be reached (reference with CBD-CdS buffer η=14.1%). In the new WEL concept without sputtered i-ZnO cells with η=14.6% (reference CdS η=14.8%) and mini modules with 10.9% (reference CdS η=12.9%) were already obtained (Fig.1).

	(a)	(b)	(c)	total area [cm²]
	ZnO:Ga	ZnO:Ga	ZnO:Ga	
	rf i-ZnO	*rf* i-ZnO		
	CBD-CdS buffer	ILGAR-ZnO WEL	ILGAR-ZnO WEL	
	CIGSSe	CIGSSe	CIGSSe	
η	14.1 %	**15.0 %**		0.5
V_{oc}	588 mV	**580 mV**		
J_{sc}	32.9 mA/cm²	**35.1 mA/cm²**		
FF	73.1 %	**73.7 %**		
η	14.8 %		**14.6 %**	0.5
V_{oc}	583 mV		**577 mV**	
J_{sc}	34 mA/cm²		**34.8 mA/cm²**	
FF	74.4 %		**72.4 %**	
η	12.9 %	mini-module	**10.9 %**	20

Fig. 1: Different structures of solar cells (upper part) and photovoltaic parameters of corresponding devices (lower part).

A broad, 100 h DH stability study of cells with CIGSSe absorbers from Shell Solar and buffer layers deposited at the HMI by various wet and dry processes revealed that ILGAR-ZnO and CBD-ZnS equally belong to the best Cd-free candidates with a relative decrease in efficiency of approx. 40%. Because this is still poorer than the CBD-CdS reference (20%), we investigated the reasons for the DH-degradation in ZnO-WEL cells.

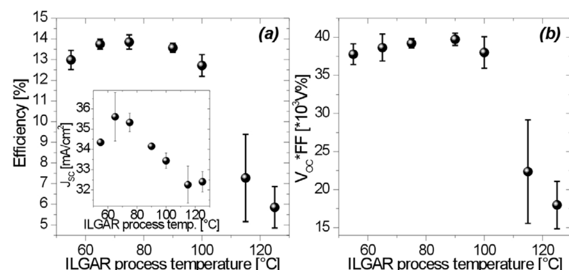

Fig. 2: Photovoltaic parameters of devices with ILGAR WELs prepared at different temperatures.

ILGAR-ZnO layers are obtained by repeating the following cycle: Dipping the substrate in $Zn(ClO_4)_2$ solution and converting the dry solid Zn^{2+}- precursor by gaseous NH_3/H_2O into the hydroxide, followed by dehydration to the oxide. Above 100°C the cell parameters strongly decrease, indicating absorber damage under the process conditions (Fig. 2). However, 100h DH tests show a better stability for 100°C than for 75°C and 55°C process temperatures (Fig.3).

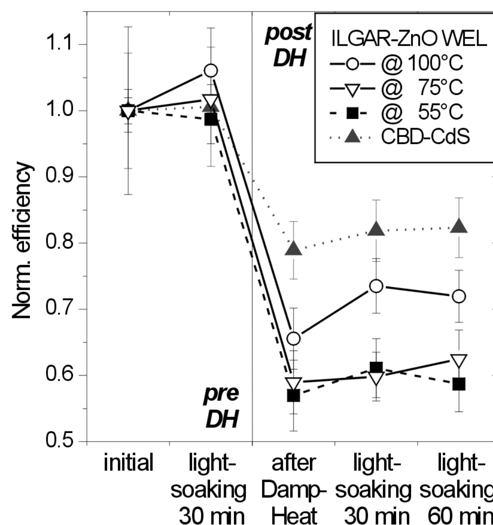

Fig. 3: Stability of the power conversion efficiency of solar cells with differently prepared WELs before (pre DH) and after (post DH) DH-test as well as after lightsoaking cycles compared to CBD-CdS buffered references.

FTIR measurements (IWF Dresden) of ILGAR-ZnO deposited at these three temperatures show a decreasing content of hydroxide from 50°C until 100°C (not detectable). As derived from XPS measurements, $Zn(OH)_2$ is converted into ZnO during DH exposure. Therefore, we conclude that the water thereby formed deteriorates the highly sensitive WEL interfaces. (Most likely this is also a reason for the degradation of CBD-ZnS having $Zn(OH)_2$ as a by-product). Consequently, for stable cells, the hydroxide content should be kept as low as possible, e.g., by high ILGAR process temperatures, but without damaging the absorber.

Ch.-H. Fischer, M. Bär, H.-J. Muffler, T. Kropp, J. Reichardt, M.C. Lux-Steiner

C. Kelch, M. Kirsch

M. Giersig, U. Bloeck

B. Leupoldt (Fraunhofer Institut Werkstoff- und Strahltechnik, Dresden);

T. P. Niesen, F. Karg (Shell Solar GmbH, München)

Preparation of wide band gap materials by structure conformal conversion

In thin-film photovoltaics, transparent semiconductors like doped SnO_2 or ZnO are used as transparent front contacts. Further demands for these materials appear in extremely-thin-absorber solar cells (eta cells). This cell concept is based on very thin but highly folded absorbers. This reduces the required degree of purity. But the absorber needs to be deposited on a transparent conductor with a highly „folded" surface. Here, new surface structures of known materials have been accessed by materials conversion.

Starting from electrodeposited columnar ZnO, which can itself be prepared in different morphologies, columnar or tubular ZnS was obtained by anion exchange in the gas phase, and further metal sulfides with the same surface structure by subsequent cation exchange in solution [1, 2]. In this step, the outer quality of the reproduced morphology depends on the interaction of the involved processes, namely dissolution, precipitation and exchange inside the solid. This was further examined by a series of Ag_2S films from increasingly higher diluted solutions, until the rate of initial precipitation no more overexceeded the overall rate of the following internal conversion [3].

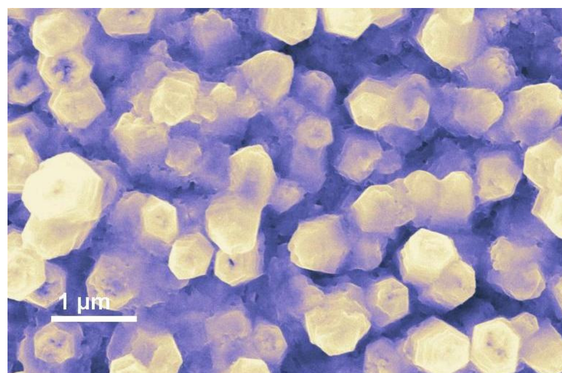

Fig. 1: columns of Ag_2S from columnar ZnS reacted with highly diluted $AgNO_3$ solution.

However, most transparent semiconductors are n-type. Only few p-type are known, e.g. CuSCN, CuI or p-conducting polymers. All those are of questionable long-term stability. Oxidic compounds have a general better stability, but only for the mixed oxide $CuAlO_2$ p-conducting behaviour has been found (on low level), and is ascribed to its exceptional layered structure (Delafossite structure, Fig 2) [4]. But this crystal phase is not the favored, most stable reaction product. Reacting the components at high temperature (around 1000°C), as well as all large-area film deposition methods, yield mainly spinel-type $CuAl_2O_4$ and Cu oxides instead.

Here, it was possible to achieve the synthesis by the structure conformal conversion of the isostructural compound α-$LiAlO_2$. Making use of the high mobility of the Cu^+ and also of Li^+ ion, a crystal structure conformal conversion of this commercially available starting material could be performed already at temperatures as low as 400°C. This scalable synthesis yields $CuAlO_2$ powder free of $CuAl_2O_4$ and Cu oxides, and allows to include dopants.

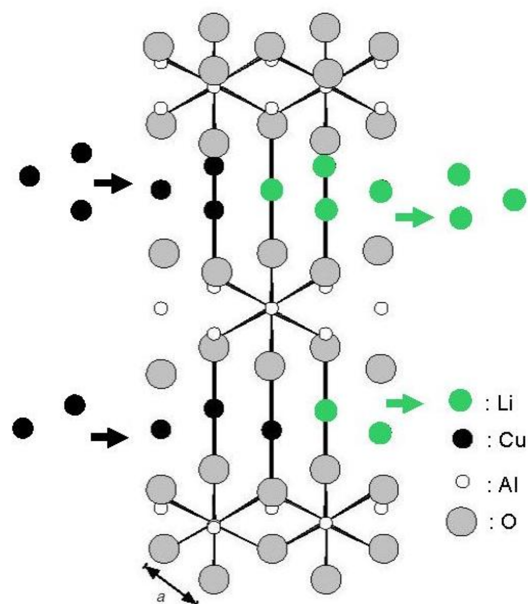

Fig 2: „Delafossite" crystal structure of $CuAlO_2$ and $LiAlO_2$, and their conversion by ion exchange in the lattice (adapted from [4])

[1] L. Dloczik, R. Engelhardt, K. Ernst, M. C. Lux-Steiner, R. Könenkamp, Sens. Act. B 84 (2002) 33
[2] L. Dloczik, M. C. Lux-Steiner, R. Könenkamp, E-MRS, Strasbourg 2002
[3] L. Dloczik, R. Könenkamp, 53th meeting of the International Society of Electrochemistry, Düsseldorf 2002
[4] H. Kawazoe, M. Yasukawa, H. Hyodo, M. Kurita, H. Yanagi, H. Hosono, Nature 389 (1997) 393

Th. Dittrich, L. Dloczik, J. Chen, R. Bayon, A. Belaidi

Phthalocyanine/C_{60} organic solar cells

We study a new type of solar cell consisting of the organics phthalocyanine and C_{60} [1] as well as buffer layers on the electrodes. The basic principle of this new type of photovoltaic devices is that of a donor-acceptor cell. Phthalocyanine plays the role of a hole-conducting donor. On the other hand C_{60} has a strong electron affinity and is under certain conditions a good electron conductor [2]. Both materials exhibit a remarkable thermal stability. This allows the processing and study of vapor deposited well-defined thin films suitable for the fabrication of organic solar cells.

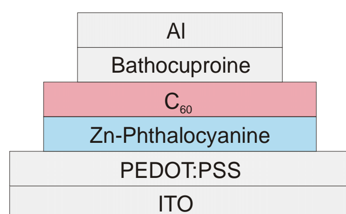

Fig. 1: Schematic cell structure. PEDOT:PSS is spin coated onto an ITO substrate. All other layers are thermally vapor deposited under high vacuum.

We fabricated this kind of photovoltaic devices in order to study charge carrier transport and electron-hole recombination at interfaces. We paid careful attention to the use of poly-3,4-ethylene dioxythiophene:polystyrene sulfonate (PEDOT:PSS) as hole-conducting and bathocuproine (BCP) as electron conducting buffer. (Fig. 1).

As front electrode we employed ITO float glass, spin coated with PEDOT:PSS from aqueous solution. The substrates were introduced into a high vacuum chamber and coated by thermal vapor deposition with Zn-phthalocyanine, C_{60}, bathocuproine and aluminum. In order to protect the cell from atmospheric oxygen it was covered on the backside with a thick C_{60} layer and then encapsulated under inert gas.

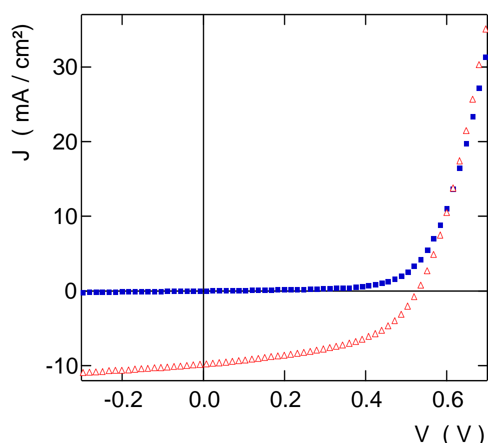

Fig. 2: I-V curve of our most efficient solar cell Triangles mark the illuminated, squares the dark measurement. Power conversion efficiency: 2.5 %.

I-V characteristics were studied under one sun AM1.5 illumination of a solar simulator. Our best devices yielded external power conversion efficiencies of up to 2.5% depending on the quality of the PEDOT:PSS layer (Fig. 2). In the case of Fig. 2 the appendant cell parameters were: J_{sc} = -9.8 mA/cm^2, V_{oc} = 0.53 V, fill factor = 0.49. The photoactive area is 3.2 mm^2. Photocurrent contribution of the active layers is shown in the external spectral quantum efficiency (ESQE, Fig. 3). ZnPc generates most charge carriers at wavelengths between 550 and 750 nm. A weaker absorption caused by C_{60} is located in the short wave part of the visible spectrum (350-520 nm). In order to study the evolution in time of ESQE, the cell was first measured immediately after the fabrication (Fig. 3, blue), then the solar cell's power conversion efficiency was determined (1.4%) under the solar simulator. After 30 minutes in the dark the second ESQE measurement (red) was recorded.

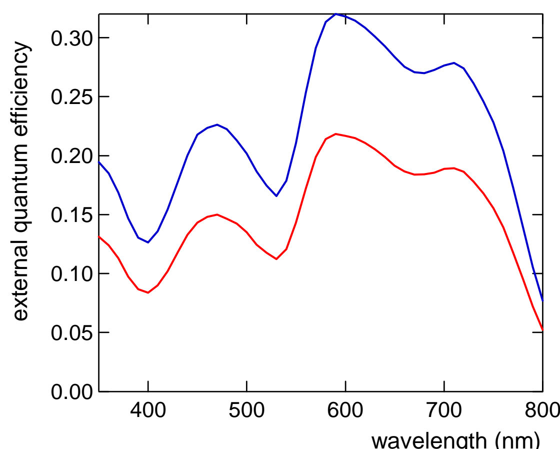

Fig. 3: After the cell's fabrication the ESQE was recorded (blue) then the power conversion efficiency was determined (1.4%). After 30 minutes another ESQE measurement (red) was recorded.

We observed an uniform decrease of the photocurrent over the whole spectrum by one third. Since the conductivity of C_{60} is strongly influenced by oxygen impurities in the film [2], we suspect that the degradation is due to oxygen, which soaks through C_{60} during the measurement in the solar simulator and to a minor degree in the dark.

[1] P. Peumans and S.R. Forrest, Appl. Phys. Lett. 79 (2001) 126
[2] R. Könenkamp, G. Priebe, and B. Pietzak, Phys. Rev. B 60 (1999) 11804-11808

K. Fostiropoulos, M. Vogel, B. Johnev, B. Mertesacker, A. Weidinger

Kelvin Probe Force Microscopy: Direct observation of electronic grain boundary properties

Kelvin probe force microscopy (KPFM) in ultra-high vacuum allows to simultaneously obtain structural as well as electronic information (work function Φ) of a sample's surface with an extremely high lateral (~ 20 nm) and energy resolution (~ 5 meV).

The application of the KPFM to a solar cell absorber material was demonstrated using $CuGaSe_2$ (E_g=1.68 eV) deposited on Mo covered glass by physical vapor deposition. In Fig. 1 (a) we present the topography image as measured with the KPFM. Clearly the various grains can be seen, with the grain size varying between 200 and 700 nm. In Fig. 1 (b) we present the simultaneously measured work function image for dark conditions. It is observed that the various grains show different absolute values of the work function. This effect was previously observed and explained by different electron affinities depending on the crystallographic orientation of the surface. Additionally, the work function is seen to decrease at the grain boundaries, as observed by the dark "rings" around the various grains.

In Fig. 2, we show the work function along the line in Fig. 1 (b). The work function is seen to drop at the grain boundaries by ~100 meV and ~170 meV, with an average of (110 ± 24) meV, when many grain boundaries are evaluated. The upper curve shows the work function along the same line for the sample measured under illumination (20 mW, λ = 685 nm). The absolute value of the work function is increased by ~ 110 meV, which can be explained by a reduced band bending at the surface. It is also apparent that the work function decrease at the grain boundaries is reduced. Averaging over many grain boundaries, the drop at the grain boundaries under illumination is found to be (76 ± 30) meV. Besides the size of the potential drop at grain boundaries, we can also extract information about the width of the space charge region (SCR) that develops at the grain boundaries. Averaging over many grain boundaries we find a SCR width of (42 ± 9) nm in dark conditions, and (56 ± 10) nm under illumination.

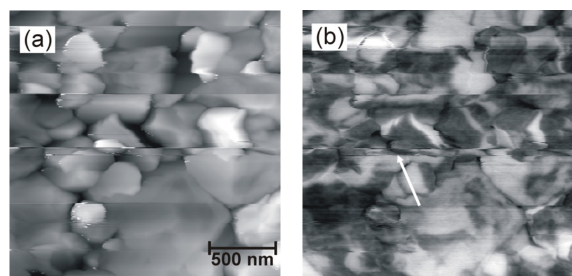

Fig. 1: KPFM measurement on $CuGaSe_2$. The topography (a) shows the grains of the polycrystalline thin film (grey scale = 360 nm). The simultaneously measured work function (b) shows a downward band bending at the grain boundaries (Φ = 4.23 – 4.39 eV). The white line gives the position of the linescan in Fig. 2.

We consider the relative changes in the work function as determined at the grain boundaries to reflect the electronic properties of the absorber material. By assuming that the grain boundary corresponds to a surface with a surface charge we determine the net doping P_{net} of the absorber material from the size of the band bending $\Delta\Phi_{gb}$ and the SCR width w, finding $P_{net} \approx 9{\cdot}10^{16}$ cm^{-3}. By the fact that the SCR width at the grain boundaries does not extend to the center of the grains, we can estimate the density of charged trap states $p_{gb} \approx 8{\cdot}10^{11}$ cm^{-2}.

We can compare these results to recent transport measurements on samples originating from the same growth process. Schuler *et al.* found $P_{net} \approx 1$ - $5{\cdot}10^{17}$ cm^{-3} for the net doping concentration, $\Delta\Phi_{gb}$ = 60 – 135 meV for the band bending at the grain boundaries and concluded the charged defect density at the grain boundary to be $p_{gb} \approx 1{\cdot}10^{12}$ cm^{2}. Whereas we analyzed a number of individual grain boundaries from our KPFM images, Schuler *et al.* investigated an "average lowest" grain boundary barrier, determined by the average barrier of the percolation path through the material. Nevertheless, the results of this study and the present KPFM study are in good agreement. The origin of the defect states at the grain boundaries can be manifold, for example dangling bonds, oxygen contamination due to air exposure, Na contamination from the glass substrate, etc.

Similar studies were also performed on the absorber material Cu(In, Ga)S_2 (E_g=1.55 eV). We do not observe a significant difference in the electronic properties at the grain boundaries between the selenide material $CuGaSe_2$ and the sulfide material Cu(In, Ga)S_2.

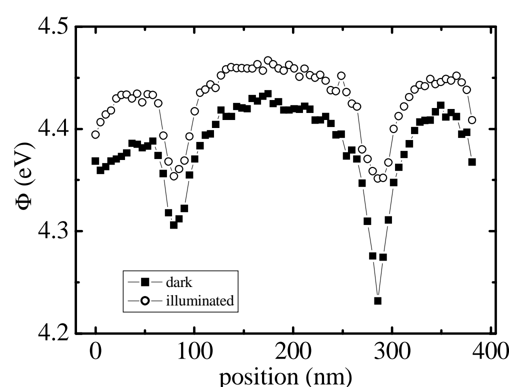

Fig. 2: Linescan along the white line in Fig. 1 (b) showing the drop in the work function at the grain boundaries. Closed symbols are for dark condition and open symbols represent the work function along the same line under illumination (20 mW, λ = 685 nm).

S. Sadewasser, Th. Glatzel, M.Ch. Lux-Steiner

Analysis of buried interfaces in $Cu(In,Ga)(S,Se)_2$ thin film solar cells by X-ray emission and photoelectron spectroscopy in the CISSY apparatus

The general aim of the CISSY project is the investigation of buried interfaces and surfaces in $Cu(In,Ga)(S,Se)_2$ ("CIGSSe") thin film solar devices. The CISSY endstation (Fig.1), completed in 2002, combines several relevant in-system preparation tools for thin layer deposition (sputter chamber, glove box for wet chemical processes) and the

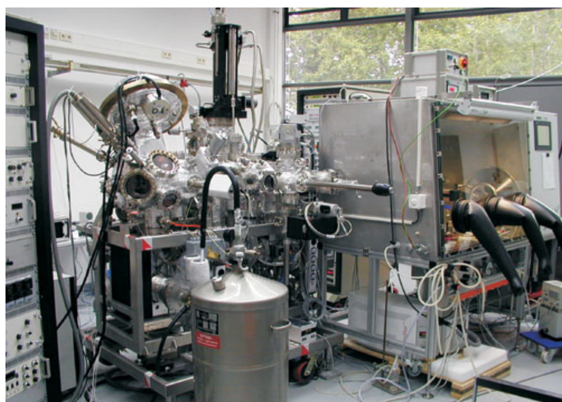

Fig.1: CISSY endstation with attached glovebox.

spectroscopic equipment for x-ray emission (XES, Scienta Gammadata) and photoelectron spectroscopy (PES, VG CLAM 4) and a variety of laboratory techniques. The analytical concept of CISSY is based on information from XES and PES on the electronic properties and the chemical composition from different information depths (XES: several 100 nm; PES: surface) for the study of buried interfaces in layer systems.

All CIGSSe absorbers stem from the pilot line of Shell Solar, and subsequent depositions of buffer layers (CdS, ZnS, ZnSe, ZnO) were performed either in the attached glovebox of the CISSY apparatus or in several labs at the HMI. Several preparation procedures were employed, including chemical bath deposition, absorber surface pre-treatments, and, in particular, the sequential cyclic ILGAR process (Ion Layer Gas Reaction) consisting of dipping and solid/gas reaction steps.

A broad study was dedicated to the stability of the CIGSSe solar cells during so-called "damp-heat tests" ("DH", 85°C/85% rel. humidity, 100 h for unencapsulated samples), a fundamental issue for the photovoltaic industry. We started with the systems ILGAR-ZnO/CIGSSe and sputtered-i-ZnO/CIGSSe, each with Cd^{2+}/NH_3 treatment of the CIGSSe absorber. In order to localize and understand the observed effects, variations of preparation conditions as well as measurements before and after damp-heat exposure were From the S $L_{2,3}$ XES spectra in Fig. 2 we learn that ILGAR-ZnO deposited on CIGSSe under air contains sulfate, the signal of which disappears after damp-heat treatment (Fig.2, left), whereas in sputter-i-ZnO on CIGSSe sulfate is observed only after damp-heat exposure (Fig.2, right). Apparently, the chemical composition and hence the electronic behavior of ZnO depends on the preparation method. One has to keep in mind

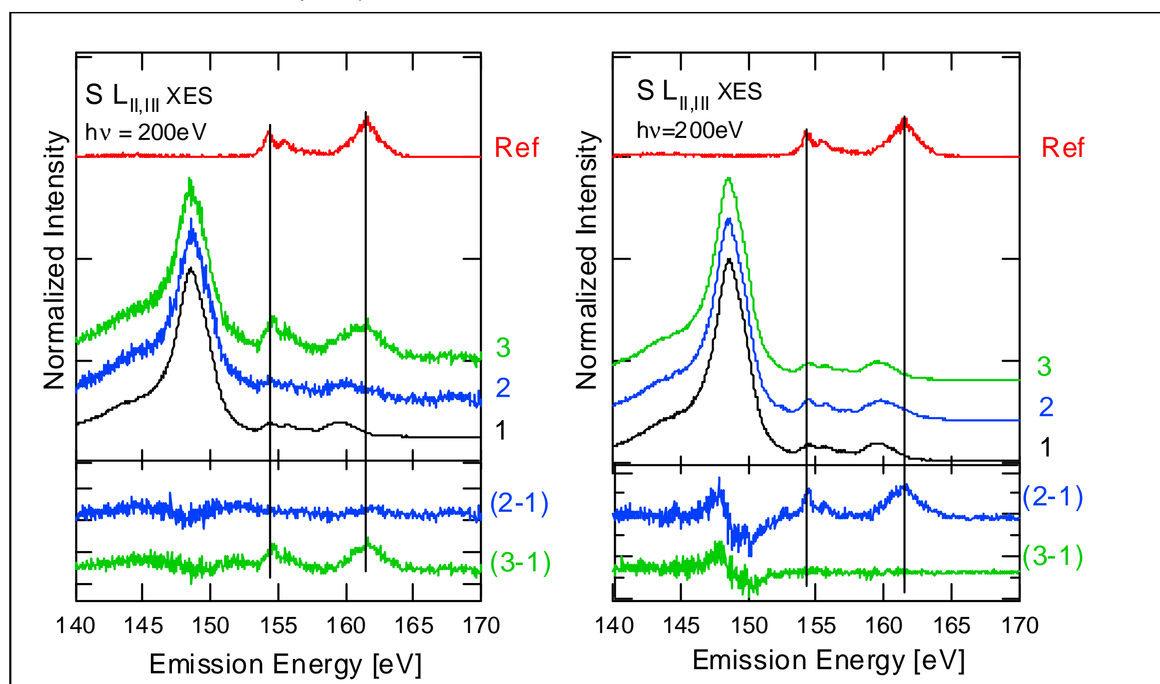

Fig.2: S$L_{2,3}$ XES spectra of 25nm ILGAR ZnO (left) and of 30nm sputter i-ZnO (right), both on Cd^{2+} treated CIGSSe as well as difference spectra and spectrum of a sulphate reference. 1: Cd-treated Absorber, 2: before damp heat test, 3: after damp heat test, Ref: $CdSO_4$.

that the sulfate represents only a small fraction of the volume analyzed by XES, i.e., that the sulfate contribution to the resulting spectrum is very small. For a better visualization of the sulfate signals, the spectra of the absorber *before* damp-heat treatment and *before* i-ZnO deposition, respectively, are subtracted from those taken *after* the respective treatments, in order to account for the large number of S atoms within a CIGSSe environment. For comparison a sulfate reference spectrum is also shown.

Complementarily, the PES spectra of the as deposited ILGAR sample give no evidence of sulfate at the ZnO surface. Therefore, the sulfate must be localized at (or near) the ZnO/CIGSSe interface. PES spectra of the same sample after DH show peaks corresponding to the absorber elements, indicating that the ZnO coverage is no longer complete, in agreement with scanning electron micrographs.

The unique CISSY feature of in-system preparation allows a preparation by wet chemical processes in the attached glovebox under N_2 atmosphere and therefore a direct comparison to products of standard preparation in air. When ILGAR-ZnO is deposited on CIGSSe in the glovebox, S $L_{2,3}$ XES spectra clearly show a reduced sulfate signal indicating that oxygen and/or humidity from the ambient environment is involved in the sulfate formation process. These results can be very important for better solar cell efficiency and stability and will be fed back directly into the solar cell production process.

Alternative ZnS buffer layers prepared by chemical bath deposition ("CBD", A. Ennaoui, HMI) have resulted in high cell efficiencies. The presence of S-Zn bonds could be confirmed by XES (Fig. 3), in spite of the small amount of material (thickness of no more than a few nm). The difference of the spectra "after minus before deposition" obtained with an excitation energy of 200 eV points to the presence of ZnS and $ZnSO_4$. However, ZnS becomes more evident by XES with deliberate excitation below the sulfate absorption edge (165 eV). Therefore, in addition to the advantage of high flux excitation, undulator-based synchrotron radiation also offers the possibility to "switch-off" a certain chemical core hole species, allowing a significantly enhanced spectral interpretation.

The present results, taken during the two inaugural beamtimes of the CISSY apparatus at the U41-PGM and the UE46-PGM beamline, give a first perspective of the multitude of information which can be obtained when combining different spectroscopic methods with in-system and, in a later stage, in-situ thin film preparation.

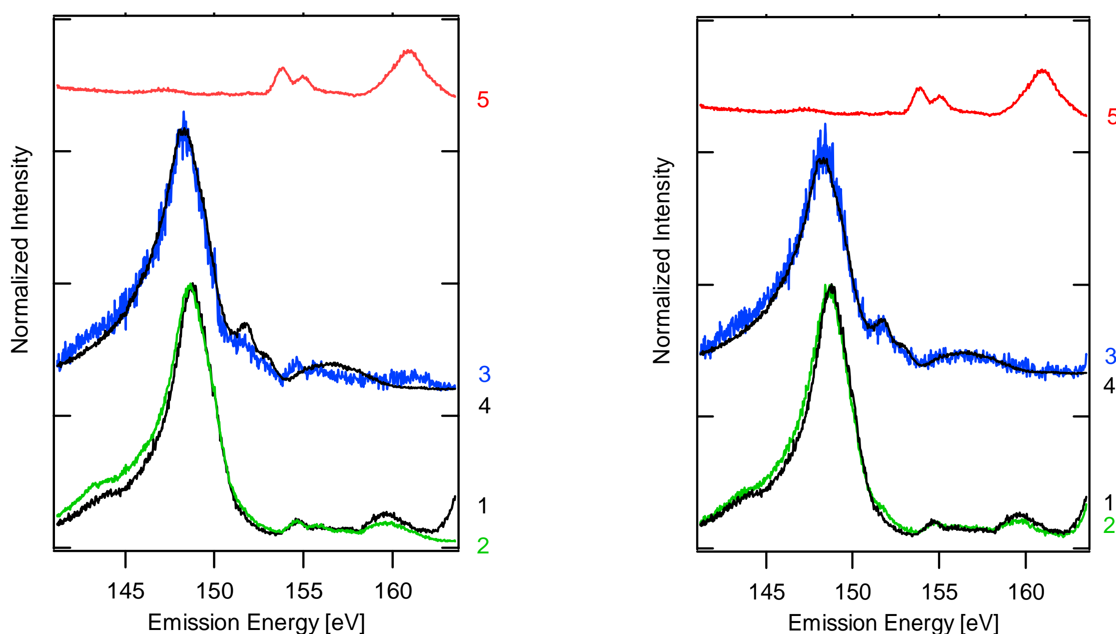

Fig. 3: S $L_{2,3}$ XES spectra of CBD-ZnS/CIGSSe, CIGSSe, and difference spectra for excitation energies of 200 eV (left) and 165 eV (right), showing the effect of deliberate excitation below the sulfate absorption edge. 1: bare CIGSSe-absorber, 2: CBD-ZnS on CIGSSe, 3: difference spectrum (2-1), 4: ZnS-reference, 5: sulfate-reference.

Ch.-H. Fischer, M. Bär, A. Grimm, I. Kötschau, I. Lauermann, J. Reichardt, S. Sokoll, and M.C. Lux-Steiner

L. Weinhardt, O. Fuchs, C. Heske, *Experimentelle Physik II, Universität Würzburg*
C. Jung and W. Gudat, *BESSY GmbH, Berlin*
T. P. Niesen and F. Karg, *Shell Solar GmbH, München*

$CuInS_2$ mini-modules - preparation and testing

Thin film solar modules of $CuInS_2$ which are prepared in an industrial relevant process are currently under development in a joint effort with the department SE2. These solar devices have the advantage over crystalline silicon devices that series connection of single solar cells to a complete module can be achieved right during processing. This integrated series connection requires the deposited layers to be cut at three different levels. According to the large area of commercial modules totally more than 100 m scribe length per level has to be performed on a single module. Thus the technology chosen for cutting the different layers not only has to be highly reliable but also fast enough to meet the production time pattern.

The first layer to be cut is the molybdenum backside metallization. A suitable procedure is laser scribing. In 2002 we have put into operation a specially designed machine consisting of a laser to cut the molybdenum layer and a stylus to mechanically cut the other two layers. The requirement of fast and reliable cuts implies the proper setting of a variety of parameters. Important parameters are laser power, laser pulse frequency and cutting speed. They all are not independent but influence one another. Complete electrical isolation can be achieved with a set of parameters in the high power regime as well as with moderate laser power. The latter has benefits in terms of the thermal strain to the molybdenum layer close to the scribeline. Fig. 1 shows a laser scribeline less than 20 microns wide in a 1 micron thick molybdenum layer.

Fig. 1: Molybdenum layer of 1 micron thickness with a laser cut less than 20 micron wide.

A scribing speed of close to 1 m s^{-1} has been realised at a isolation resistance of >10^6 Ω. First mini-modules including laser-cut molybdenum have been fabricated. However, fine adjustment of the parameters is still ongoing.

In collaboration with SE2, the routine preparation of mini-modules in a so-called baseline has been strongly intensified. The ultimate goal is to test the baseline at a throughput of 20 mini-modules per months. Module efficiencies up to 9.7 % could be achieved on 5x5 cm^2 glass substrates (aperture area efficiency, independent measurement by FhG-ISE, Freiburg). Up to now, not all of the modules reach top efficiencies, there are also devices that show poorer performance. In order to discover the reasons for unsatisfactory performance these modules have been analysed in order to reveal defect mechanisms. By application of our infrared camera system shunts could be revealed as a major loss mechanism. Electrical current is passed through the solar device which leads to Joule heating of every cell of the module. As shunts tend to focus this current, local heating will occur which can be detected by the camera. Using lock-in technique this infrared camera is able to discriminate lateral temperature differences on a sample in the sub-mK range.

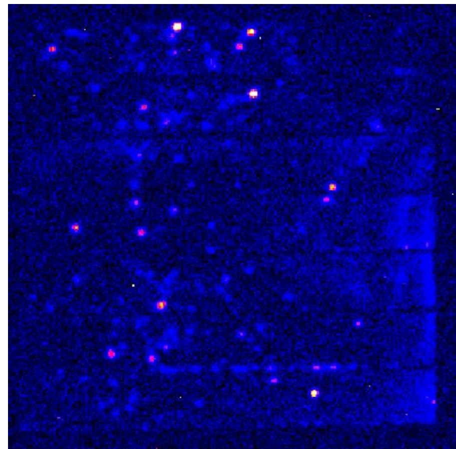

Fig. 2: Thermography image of a mini-module with 9.7 % efficiency and 66.6 % fill factor. The brighter the colour, the higher the local temperature.

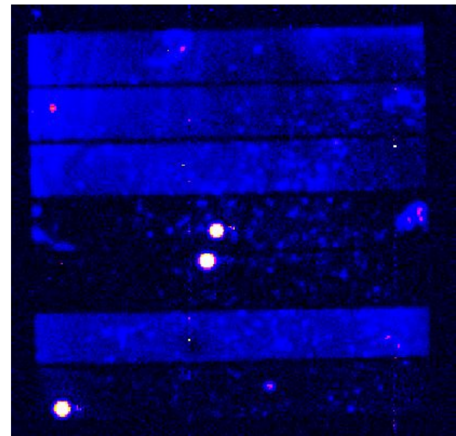

Fig. 3: Thermography image of a mini-module with 8.6 % efficiency and 59.2 % fill factor. Three hot spots are due to small local shunts. As in a series connected module the current through all cells must be the same the shunted cells show darker because part of the current in these cells is concentrated at the shunt paths.

Fig. 2 and 3 show thermography images taken of two modules of unequal performance. While the module in Fig. 2 with 9.7 % efficiency and 66.6 % fill

factor shows almost homogeneous temperature distribution over the entire module area, the infrared image of the less efficient module reveals three hot spots, which are caused by small local shunts. Delamination of the absorber layer in the vicinity of the scribe line has been identified as a major cause for shunts. This problem could be reduced by changing the dimensions of the interconnect pattern. The infrared camera system has thus turned out to be a powerful tool for quality control and failure analysis.

Solar modules for outdoor application have to be protected against environmental influences. To this end, the devices are often encapsulated by laminating a second glass plate onto the thin film layer structure. This procedure has been performed using a ethyl-vinyl-acetate (EVA) foil. Attention has to be paid to the lamination temperature: on one hand to fulfil the requirements of sufficient polymerisation, on the other hand not to degrade the device. Other important parameters are lamination pressure and time. The critical regions of the modules are the edges since there is only a small rim to seal glass on glass and where humidity can penetrate into the layers. This small rim is necessary in order to obtain as much active device area as possible.

Alternative procedures have been considered in order to facilitate the encapsulation process. A very simple method has been developed by the department SE5 and has been evaluated in co-operation. An organic wax of natural provenience is deposited by dipping the module into a solution of the wax. These wax sealed modules are tested without an additional cover by a second glass plate.

Fig. 4: $CuInS_2$ mini-modules at the test array on the HMI campus (near the guesthouse) exposed to the Berlin weather.

The encapsulated modules have been exposed to several stress tests to examine their stability and to evaluate the reasons of possible degradation. Modules have been exposed to Berlin weather since October 2002 at a new experimental test array close to the guesthouse. This test array which has a capacity of up to 20 modules of different sizes has been developed together with SE2. During 3 months of field exposure, the laminated modules exhibited a degradation of only 5% in efficiency. The wax sealed modules did not show a stronger degradation than the glass laminated ones.

A standardised method for time-accelerated tests for solar modules is the so-called ISPRA-test (IEC 1215). Under this test, modules are stressed for 1000 hours at 85 °C and 85 % relative humidity (damp-heat). In order to provide this widely used standard test procedure, a new climate exposure test cabinet was put into operation in December 2002. Fig. 5 depicts the relative efficiency of 3 modules as a function of exposure time to the damp-heat test. The module (a) in Fig. 5 has been exposed without any protective cover and serves as a reference. Within 200 h, the efficiency of this device deteriorated to 20% of its initial value. It should be noted that degradation in 85°C dry atmosphere on the contrary is negligible. Thus, the strong degradation of the uncovered module emphasizes the importance of sealing against humidity. The physical mechanism of degradation is not known so far. Both encapsulated modules (b) and (c) in Fig. 5 exhibit a decreased degradation with respect to the non-excapsulated one. Again the wax sealed modules behaved similar to the glass encapsulated ones. Nevertheless, the degradation is still much larger than required in order to pass the ISPRA test. Further work has to concentrate on 2 aspects of this type of stability: (i) improved inherent stability of the solar cells to humidity and improved encapsulation and/or sealing.

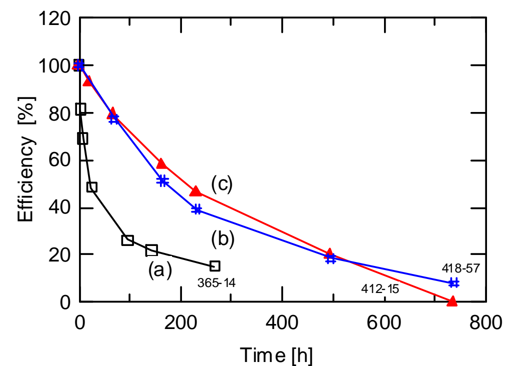

Fig. 5: Degradation of the efficiency of a non-encapsulated (a), a glass-encapsulated (b), and a wax covered (c) module under climatic test at 85 °C and 85 % relative humidity.

J. Klaer, I. Luck, A. Boden, A. Werner, I. Gavilanes-Perez, R. Klenk, R. Scheer

$CuInS_2$ quality assessment by Raman spectroscopy

It is well known that Raman scattering can qualify the perfectness of materials such as thin films. The goal of this work is to develop Raman scattering as a quality control for $CuInS_2$ solar cell production. Our group, in collaboration with the university of Barcelona, previously investigated Raman spectroscopy for $CuInS_2$ thin films (see HMI Annual Report 2001 SE3.01b). Samples with different structural quality, as it results from Cu-poor compared to Cu-rich preparation, has been studied. It was found that films of Cu-poor stoichiometry or those formed at significant too low substrate temperature exhibit a defect ordering, the so-called CuAu ordering. Absorbers prepared in our baseline grow under Cu-rich conditions and show only a small or even no content of that CuAu ordering. In-situ Raman spectroscopy performed during the growth of the films, however, revealed that the CuAu ordering marks an intermediate state of crystallisation.

In order to investigate the baseline $CuInS_2$ films by Raman scattering and to derive further relations between spectroscopic features and photovoltaic performance, a large number of samples has been investigated. They were prepared under different conditions, e.g. variation in process temperature, Cu/In-ratio and absorber thickness, and completed to working solar cells. All samples have in common that a dominant Raman mode (A_1-mode) can be observed which is caused by the vibration of the anion sublattice. As already known from other materials the FWHM (full width at half maximum) of a Raman peak is an indicator for crystal quality, i.e. the density of localised and extended defects, of a material. Therefore, the aim of the current work is to find a correlation between the signature of the A_1-mode and the solar cell parameters.

Fig.1 shows Raman spectra of three representative samples together with the fit results. As can be seen, the dominant Raman mode appears at approximately 292 cm^{-1} corresponding to the A_1-phonon mode of $CuInS_2$. No contribution of the CuAu related mode at 305 cm^{-1} could have been detected.

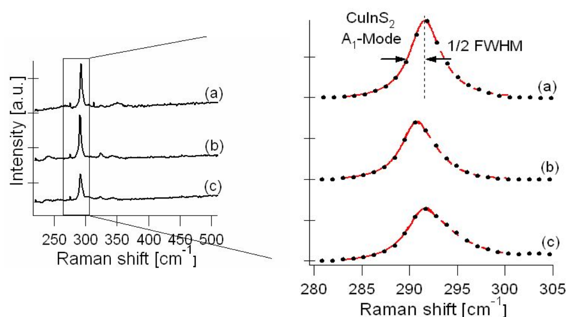

Fig. 1: Raman scattering intensities versus wavenumbers for different Glass/Mo/$CuInS_2$/CdS/ZnO samples. Primary and scattered light of the Raman experiment were passing the window layer of ZnO/CdS. The dots represent the measured data, the full line the symmetric fit. Open circuit voltage : (a) 726 mV, (b) 651 mV and (c) 194 mV

The spectra shown are characterised by different spectroscopic broadening (FWHM values), where the large FWHM of spectrum (c) can be appreciated by the naked eye. This sample has been measured with a V_{oc} (open circuit voltage) of below 200 mV. As already implied by Fig.1, a decrease in V_{oc} values (from samples (a) to (c)) is correlated with an increase in FWHM of the A_1-mode.

In Fig.2 the solar cell parameter V_{oc} of numerous solar cells is plotted as a function of the determined values for FWHM of the dominant Raman mode. Up to a FWHM of 3.5 cm^{-1}, values for V_{oc} of 0.7 V or above have been found. In the range of 3.5 to 4.0 cm^{-1} the data of V_{oc} show a scattered behaviour (between 0.7 and 0.54 V) which seems to have a slightly decreasing tendency. But below 4.0 cm^{-1} a significant decline in the values for V_{oc} can be stated. Thus we interpret the data as suggested by the dashed line in Fig.2. According to the experimental relation between V_{oc} and Raman line width, a quality condition of FWHM < 3.5 cm^{-1} can be formulated. This condition now qualifies the absorber material as such before testing it in a complete solar cell.

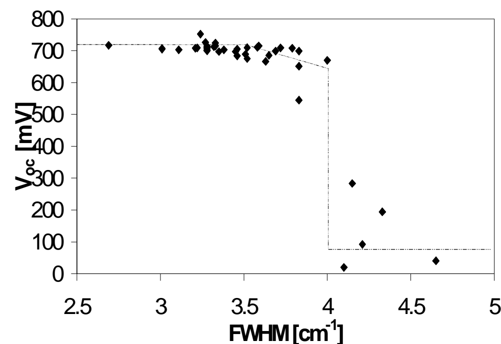

Fig. 2: Open circuit voltages of solar cells versus the FWHM of the A1 mode.

Raman peak broadening can be explained by high defect densities in the lattice. Although little is known about the specific type of defects in our films, we assume the same relationship to explain our results. The decreasing V_{oc} can be interpreted as a result of higher defect densities: The V_{oc} of a solar cell depends logarithmically on the saturation current j_0. If we assume that for $CuInS_2$-based solar cells the main recombination path appears in the space charge region, a direct correlation exists between the density of the recombination sites N_t and j_0. Therefore, V_{oc} is expected to be reciprocal to $\ln(N_t)$. This indeed has been found by admittance spectroscopy. Thus, crystal defects seem to be the limiting factor for the V_{oc} for FWHM values larger than 3.5 cm^{-1}. But as indicated by the saturation behaviour of V_{oc} for low FWHM values, crystal defects cannot be the only limiting factor. Obviously there are other limitations which reduce the V_{oc} below the predicted theoretical value of 1V.

E. Rudigier, I. Luck, R. Scheer

A new application of NOPA: Generation of sub-20 femtosecond laser pulses in the visible and near infrared at 100 kHz repetition rate

A novel 100 kHz Nonlinear Parametric Optical Amplifier (NOPA) for the generation of sub-20 femtosecond laser pulses was developed and successfully installed. The new apparatus provides shorter and better tunable laser pulses than commercially available NOPAs that run at only 1 kHz. Femtosecond Transient Absorption and Two Photon Photoemission measurements at semiconductors require low level laser excitation keeping signal detection in an acceptable linear range. This is achieved here via the high repetition rate of 100 kHz. The new device represents thus a significant improvement towards time-resolving the dynamics of hot charge carriers at the surface and in the bulk of III-V materials and verifying theoretical models. In addition the still lasting controversy regarding electron injection times in dye sensitized solar cells can now be solved making use of the better time resolution and tunability. The new device was planned and designed in collaboration with the group of Prof. E. Riedle at the LMU in Munich. So far NOPAs have only been used with 1 kHz Ti:sapphire pump systems and pump energies above 100 µJ [1]. The low energy pump (5 nJ) required a careful optimization of the setup. The NOPA is adjustable from 460 nm to well beyond 1 µm (Fig. 1). At the maximum of the tuning curve a pulse energy of 750 nJ was obtained corresponding to a quantum efficiency of more than 30 % from the blue and an overall energy conversion efficiency (800 nm to green) of about 10 %. The average power of 75 mW is considerably higher than that obtained from comparable commercially available 1 kHz systems with sub-20 fs pulse length.

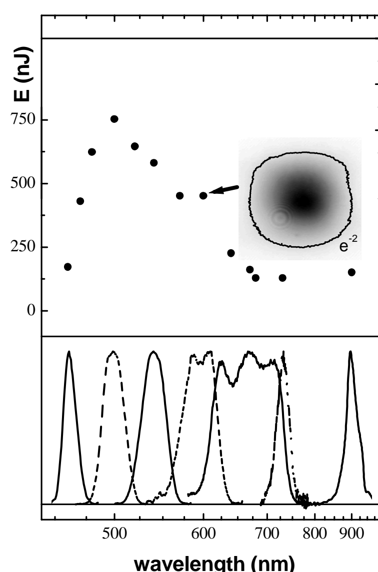

Fig.1: Pulse energies and spectral performance of the NOPA. The inset shows the beam profile at the output at around 600nm.

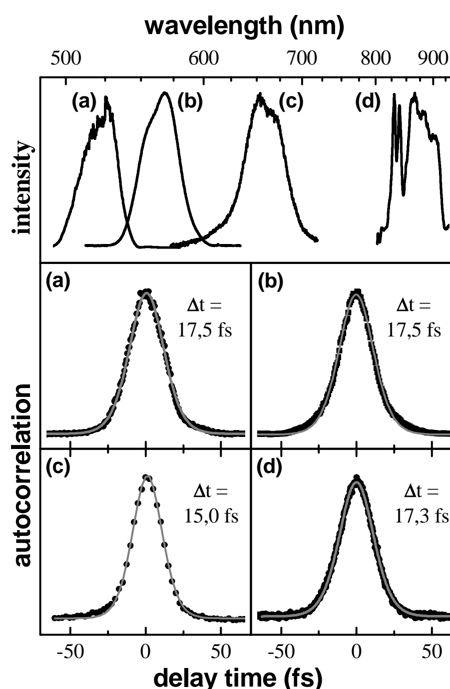

Fig.2: Autocorrealation traces and $sech^2$ fits with corresponding spectral bandwidths

Fig. 2 shows the laser pulse width measured in an autocorrelation setup with a SiC diode as two-photon mixing device. Similar results were obtained when a thin BBO crystal was used for mixing. The pulses were recompressed in a quartz prism compressor assembly. The spectral bandwidths should allow for even shorter pulses in more sophisticated compression setups.

Reference

[1] E. Riedle, M. Beutter, S. Lochbrunner, J. Piel, S. Schenkl, S. Spörlein, W. Zinth, Appl. Phys. B **71** (2000) 457.

R. Eichberger, L. Gundlach, R. Ernstorfer,
C. Zimmermann, F. Willig

Experimental proof of electron injection with finite lifetime from the exited perylene chromophore anchored on TiO_2 with a carboxyl group

Ultra-fast photo-induced electron transfer from large molecular adsorbates into semiconductors is firstly an interesting fundamental case study [1] and secondly of considerable importance for some application-oriented devices, e.g. unconventional dye sensitized solar cells [2]. The dynamics of electron transfer from a photo-excited molecular donor state into the conduction band of a nano-structured film of TiO_2 anatase was studied with transient absorption spectroscopy.

It is important to distinguish between two border cases of ultra-fast heterogeneous electron transfer, i.e. a direct optical transition or a transition from the first optically excited state (finite lifetime) of the adsorbed dye molecule. The different oscillator strengths involved require a different amount of adsorbed dye necessary for absorption saturation and hence also influence the recombination time constant via the thickness of the light absorbing layer.

The strength of electronic coupling is reflected in the degree of mixing between excited molecular states and unoccupied electronic levels of the semiconductor. In the first case of strong coupling, which is given for small molecules directly bound to a semiconductor surface, the corresponding electron transfer times can be faster than 3 fs [3] with an energy uncertainty above 0.5 eV. The effect of vibrational excitation of the molecular donor is nearly washed out, and new states may arise in this strong coupling case. Photo-excitation of such so-called charge transfer states results in a direct optical transition from a localized molecular to a delocalized bulk state [3]. In the second case of weak to moderate electronic coupling typical electron transfer times are several ten to a few hundred femtoseconds.

The influence of vibrational wavepackets on heterogeneous electron transfer dynamics has been studied in such systems with laser pulses of e.g. 20 fs duration [4].

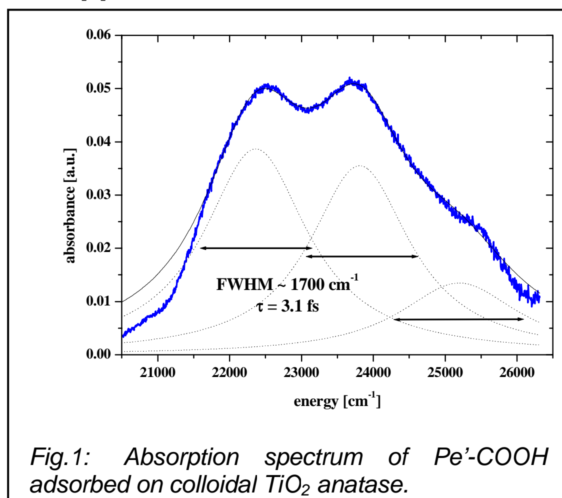

Fig.1: Absorption spectrum of Pe'-COOH adsorbed on colloidal TiO_2 anatase.

We have varied the electronic coupling between a chromophore, i.e. perylene, and the surface of TiO_2 in a systematic fashion by inserting different molecular spacer groups with saturated bonds [5]. Fig.1 shows the absorption spectrum of 2,5-Di-tert.butyl-9-perylenyl-carbonic acid (Pe'-COOH), the perylene derivative with the strongest coupling, attached to colloidal TiO_2 anatase. The vibrational signature of the non-adsorbed chromophore is conserved, indicating the absence of very strong coupling that is often attributed to a direct opticalcharge transfer transition to bulk states. From the maximum linewidth compatible with the spectrum one can determine a minimum injection time longer than 3 fs.

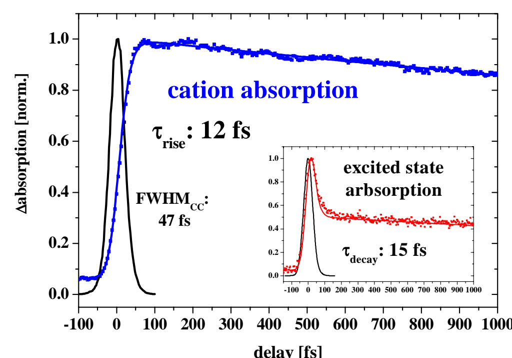

Fig.2: Transient absorption of Pe'-COOH on TiO_2 after photo-excitation with a 30 fs laser pulse: The rise of the cation signal (blue) and the decay of the excited state absorption (inset) indicate an injection time constant of 12 fs and 15 fs, respectively.

A direct measurement of the transfer dynamics is shown in Fig.2. The rise of the molecular product state, i.e. the perylene cation, was monitored at 570 nm after excitation with a 430 nm pump pulse (FWHM of the cross-correlation: 47 fs). The solid line shows the fit of the mono-exponential rise with a time constant of 12 fs. The inset shows the decay of the photo-excited singlet state (probe wavelength: 710 nm), which contains equivalent information. Excited state and cation dynamics agree well within the experimental uncertainty and give a proof of the finite injection time in the strong coupling case that is realized by attaching perylene via a carboxyl group onto TiO_2.

References

[1] S. Ramakrishna, F. Willig, V. May, Phys. Rev. B 62 (2000) R16330.
[2] B. O'Regan and M. Grätzel, Nature 353 (1991) 737.
[3] J. Schnadt, B.A. Brühwiler, L.Patthey, J.N. O'Shea, S. Södergren, M. Odelius, R. Ahuja, O. Karis, M. Bässler, P. Persson, H. Siegbahn, S. Lunell, N. Martensson, Nature 418 (2002), 620.
[4] C. Zimmermann, F. Willig. S. Ramakrishna, B. Burfeindt, B. Pettinger, R. Eichberger, W. Storck, J. Phys. Chem. B 105 (2001), 9245.
[5] R. Ernstorfer, S. Felber, L. Gundlach, C. Zimmermann, R. Eichberger, F. Willig, in preparation.

R. Ernstorfer, W. Storck, S. Felber, L. Gundlach, S. Ramakrishna, C. Zimmermann, R. Eichberger, S. Kubala, L.Töben, F. Willig

In-situ Control of MOCVD grown GaSb(100)

GaSb is a low bandgap semiconductor that is of great interest for novel solar cell devices, i.e. firstly for thermo- photovoltaic cells and secondly for high efficiency multi-junction solar cells. It is well known that the growth of GaSb is more complicated and puts more restrictions on the growth parameters (gas pressures, temperature) than other III-V materials like GaAs and InP. In-situ monitoring of MOCVD (metalorganic chemical vapor deposition) growth is a key issue since it can lead to a better control over the growth of the semiconductor layer. Reflectance difference/anisotropy spectroscopy (RDS/RAS) is a powerful tool for performing this in-situ monitoring of III-V-semiconductor growth in an MOCVD reactor. This technique delivers optical spectra that show unique spectral features for different materials, surface properties and even can give information on dopant concentration. Once the relation between the RDS signals and the material properties is known, these 'fingerprint' signals can be used to monitor and optimize the growth process. RDS is a reflectance technique that probes the anisotropy arising from the different atomic structure on the surface compared to an isotropic bulk. It measures the difference in the normal-incidence reflectance $\mathbf{r}_{[-110]}$ and $\mathbf{r}_{[110]}$ of linear polarized light that impinges at normal incidence onto the sample. This difference is normalized to the total reflectance <r> (Fig.1). The RDS signal arises due to a reduction in symmetry on the reconstructed surface. RDS signals can originate also from anisotropic atomic steps, terraces, and 3D structures of micrometer dimensions.

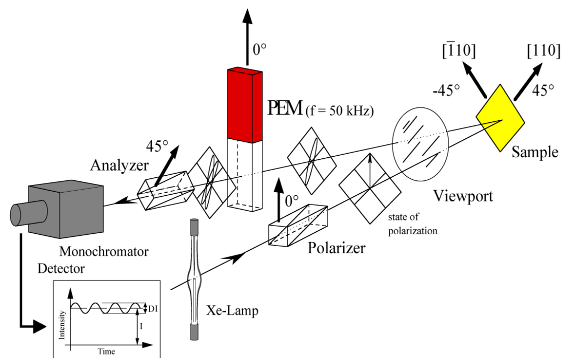

Fig.1 Experimental set-up for RDS/RAS measurements according to [1]: The difference in reflectance is measured employing the lock-In technique. Diagram from J. Rumberg, TU Berlin (1995)

Epitaxial GaSb(100)-semiconductor films were prepared in an AIXTRON AIX-200^{TM} reactor using triethylantimony (TESb) and triethylgallium (TEGa) as precursors. Sample growth was monitored in the MOCVD reactor with RDS. Fig. 2a shows the RDS spectra of a successfully grown GaSb sample. It is also the first published application [2] of the recently introduced RAS apparatus that allows for measurements in the near IR spectral range (0.8 eV to 5.0 eV).

With unfavorable parameters (high flow rates or unsuitable Sb/Ga-ratios) the growth of anisotropic 3D islands of micrometer dimensions was promoted (Fig. 2b). The occurrence of the latter led to a strong RDS signal. Compared to a flat surface these islands led to an increase in the RDS signal by more than one order of magnitude. The growth of such 3D islands was avoided by the choice of appropriate growth parameters (Fig.2a). State of the art GaSb films were grown with residual charge carrier concentrations $N_p < 3 \times 10^{16}$ cm^{-3} under appropriate growth conditions (V/III-ratio=1.55, $p_{TEGa} < 7 \times 10^{-4}$ mbar, growth rate=1.6 µm/h, T=550°C).

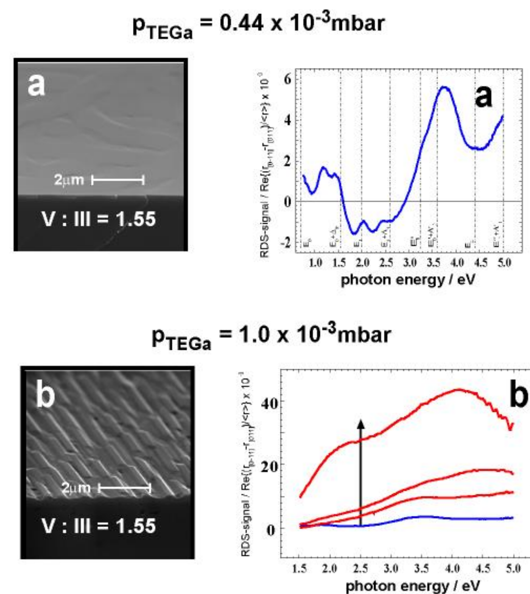

Fig.2 a) RDS signal of GaSb(100) and electron microscope image of the surface for proper growth conditions. b) GaSb(100) grown with unfavorable growth parameters: The extremely strong RDS signal originated at 3D structures that were oriented parallel to the [-110]-axis.

Reference

[1] D.E. Aspnes, J.P. Harbison, A.A. Studna, L.T. Florez, and M.K. Kelly J. Vac. Sci. Technol. A6 (1988) 1327

[2] K. Möller, Z. Kollonitsch, Ch. Giesen, M. Heuken, F. Willig, T. Hannappel J. Crystal Growth 248 (2003) 244

K. Möller, Z. Kollonitsch, H.-J. Schimper, T. Hannappel, F. Willig

Energies of unoccupied and occupied electronic surface states on In-rich (2x4)-reconstructed InP(100) measured with femtosecond 2PPE

The pioneering work of Bokor and Haight [2] has established that time-resolved two-photon-photoemission (2PPE) is a powerful tool for elucidating the existence and energetic positions of unoccupied electronic surface states or interface states in the band gap, and also of surface and interface resonances, where the latter are isoenergetic with bulk states in the conduction band. It is at hand to employ this powerful tool for investigating materials of technological relevance, in particular III-V semiconductors for solar energy conversion grown via MOCVD (metalorganic chemical vapor deposition). It is meaningful to test these sometimes complicated 2PPE signals first at a well-defined surface where valuable supporting information concerning the atomic structure on the surface can be collected by applying many different tools of surface science. In addition it is helpful when experimental results can be compared with theoretical predictions. All these criteria are met by the (2x4)-reconstructed In-rich surface of InP(100). Electrons lifted by a laser pulse to an unoccupied electronic state are not stable at this energy level and will scatter with other charge carriers and phonons thereby reaching unoccupied electronic levels at lower energies. Such processes occur in femtosecond time windows. Thus, measurements of meaningful 2PPE spectra require laser pulses of femtosecond duration. Photons in the probe laser pulse must have sufficient energy to lift the electrons from the unoccupied electronic states in the solid into vacuum where they are recorded and analyzed for their kinetic energy and angular distribution.

Fig. 1 shows the 2PPE spectrum (solid curve) of the clean ordered (2x4)-reconstructed In-rich surface of InP(100) measured with 4.66 eV photons and pulse widths below 50fs (FWHM) [2]. The origin of the peaks was elucidated in additional measurements where e.g. the photon energy and polarization of the pump pulse was varied. It was found that i_4 stems from occupied surface states located close to the upper edge of the valence band as had been seen also with UPS. Peak i_3 stems from a bulk state, and i_2, i_1 originate at unoccupied surface resonances. The rise in the signal at kinetic energies corresponding to photoemission from the band gap, i.e. below the conduction band minimum (CBM in Fig.1), was attributed to defects that are inhomogeneously distributed over the surface, probably tiny cluster of Indium. Preparation of the ordered (2x4)-reconstructed In-rich surface involved temperatures above 360°C, where phosphorus is preferentially desorbed from the crystal lattice. It is well known that a large concentration of Indium droplets can easily be formed on this surface at elevated temperatures. In agreement with this scenario this part of the signal was not observed on the ordered (2x1/2x2)-reconstructed P-rich surface of InP(100). The uppermost layer of the latter is made up of only phosphorus atoms. It is highly unlikely that Indium clusters or droplets can be formed on this surface.
The peaks ascribed to the surface states were strongly diminished (Fig.1) after the surface had been exposed to hydrogen. The two unoccupied surface states i_1 and i_2 are located 0.2 eV and 0.85 eV above the conduction band minimum, respectively. Our experimental findings are in excellent agreement with theoretical predictions by Schmidt et al. for this surface reconstruction of InP(100) [3]. The obvious next task will be time-resolving the dynamics of hot electrons on this surface, i.e. measuring in real time electron scattering between surface resonances and bulk states in the conduction band.

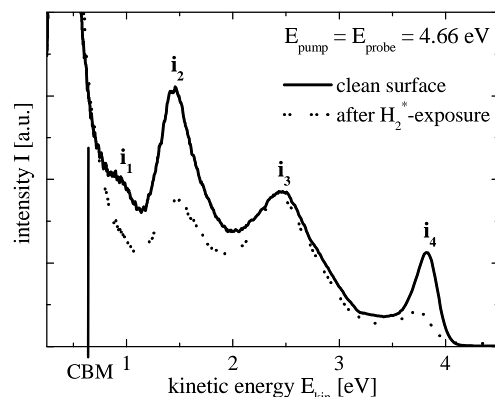

Fig.1: 2PPE-spectrum (4.66 eV photons) of the ordered (2x4)-reconstructed In-rich surface of InP(100) before (solid curve) and after (dotted curve) exposure to excited hydrogen.

References

[1] R. Haight, Surface Science Reports 20 (1994) 276

[2] L.Töben et al., J. Cryst. Growth 248C (2003) 206

[3] W.-G.Schmidt et al., Phys. Rev. B 61 (2000) R16335

L. Töben, R. Eichberger, L. Gundlach,
T. Hannappel, R. Ernstorfer, F. Willig

Electrochemical Surface Conditioning

Electrochemical methods are increasingly used because of their high specificity allowing potential, current and charge control. For semiconductor surface modification of photovoltaic absorbers, changes can be made from the submonolayer range up to several micrometers as will be shown below. The initial stages of roughening of float-zone n-Si(111) could be investigated according to Fig. 1 where a photocurrent-voltage and the current behaviour with time are shown schematically; interruption of the conditioning procedures are marked by labels (A) and (a) – (c). After sample emersion from the electrolyte at potential (A), the surface was analysed by synchrotron radiation photoelectron spectroscopy (SRPES)(Fig. 2). The conditions (a) – (c) were investigated by atomic force microscopy (AFM) (Fig. 3).

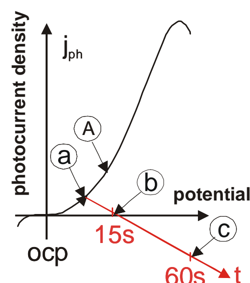

Fig. 1: Schematic photocurrent-voltage and photocurrent-time behaviour of n-Si(111) in 0.1 M NH_4F including emersion times amd potentials (see text).

Fig. 2: Si 2p line including deconvolution obtained after sample emersion at position (A) in Fig. 1.

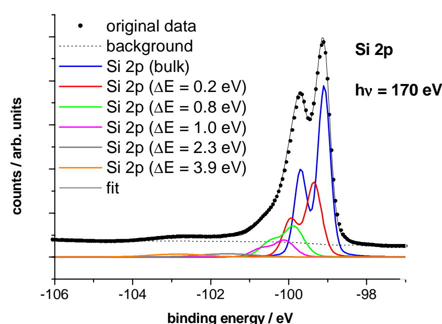

Fig. 2 shows the Si 2p core level line after emersion (see (A) in Fig. 1) only slightly positive of the rest potential (ocp) in the NH_4F solution. The original data have been fitted by mainly 5 contributions which exhibit shifts in binding energy E_b with respect to the so-called bulk line at E_b = -99.2 eV and are characterised by different areas. From comparison with density functional theory calculations made for expected reaction intermediates at the surface, the following assignments can be made; H-termination (ΔE=0.2 eV), =Si-H-OH (ΔE=0.8 eV) and =Si-H-F (ΔE=1.0 eV) species and a precipitate (ΔE=2.3 eV).

The AFM images show the onset of the dissolution process at step edges of atomic terraces (Fig. 3a) with formation of nanometer-sized pits. The images demonstrate that the initial progress in pit growth (Fig. 3b) occurs rather in lateral than in vertical direction. For increased dissolution charge, rather regular features (Fig. 3c) develop which exhibit large flat mesa-type islands.

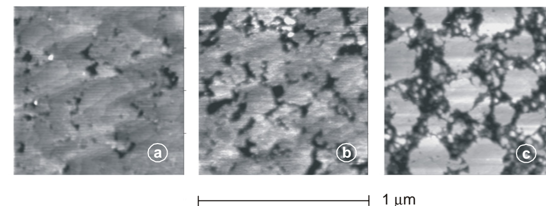

Fig. 3: AFM micrographs of n-Si(111) obtained after emersion at potential and times labelled (a)-(c) in Fig. 1. Dissolution charge: 0.28 $mCcm^{-2}$ (a), 0.69 $mCcm^{-2}$ (b), 4.5 $mCcm^{-2}$ (c).

In 0.2 M solution, the dissolution current is considerably higher (AFM images not shown) and the analysis of the 3-dimensional roughness shows a hitherto unknown exponential relationship with the charge passed upon dissolution. The understanding of the selective roughening serves as a prerequisite for directed nanostructure formation for light coupling and photonic devices.

The elctrochemical conditioning of $CuInS_2$ solar cell absorbers covered with a deleterious CuS phase has been partly successful as shown in Fig. 4. After a treatment at cathodic potential (reduction of CuS) the photocurrent-voltage characteristic in a photoelectrochemical (PEC) solar cell with $V^{2+/3+}$ redox electrolyte is compared to the one obtained after the poisonous KCN etch. The lower performance of the electrochemically treated sample is attributed to Cu_2S remnants acting as shunts as evidenced by recent X-ray emission spectroscopy measurements at BESSY II. New conditioning procedures are currently tested.

Fig. 4: PEC solar cell characteristics of electrochemically (red) and KCN etched (black) $CuInS_2$

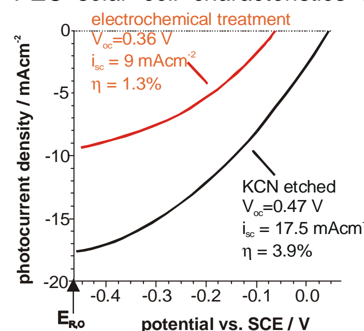

H.J. Lewerenz, H. Jungblut, M. Aggour, J. Jakubowicz, C. Murrell, M. Kanis, M. Gaul

Charge carrier kinetics in the space charge region

The interface Si_3N_4/Si is of large practical and theoretical importance. On the practical side the application in MOSFETs, as energy converting interface, antireflection system [1] in solar cells and as electronic passivated Si surfaces in Si devices [1] can be mentioned. On the theoretical side the Si_3N_4/Si interface can be considered as one of the most simple forms of a hetero junction and so it can be used as a model system for the study of the behaviour of hetero junctions.

The Si_3N_4/Si interface is characterized by a high fixed, positive charge density (about $2x10^{12}$ cm^{-2}) in the Si_3N_4 part compensated mainly by free electrons in the Si part of the junction . So at the Si_3N_4/p Si heterojunction an inversion layer is built up. It is reported that the mobility of minority carriers (i.e. electrons) in the inversion layer is strongly reduced down to 250 $cm^2V^{-1}s^{-1}$[2]. Excess charge carrier kinetics in silicon wafers is described by recombination and trapping of excess charge carriers in the volume and at the surface. Generally surface processes are taken into account by defining an effective surface recombination velocity at the edge of the surface space charge region. Volume recombination is mostly represented by a simple volume recombination time although trapping may occur. However, also the separation and storage of excess charge carriers in the space charge region must be taken into account .

In this work the influence of the pSi/Si_3N_4 interface on excess charge carrier kinetics in the pSi substrate has been studied by contactless transient photoconductivity measurements. Substrate wafers of different resistivities have been investigated. Furthermore, the difference between samples at one face and at both faces coated with a Si_3N_4 film has been studied.

Contactless and non-invasive transient photoconductivity measurements in the microwave frequency range were performed at 10GHz with the Time Resolved Microwave Conductivity (TRMC) method in an equipment as described previously [3]. The TRMC signal, i.e. the relative change of the microwave power reflected from the sample upon illumination, $\Delta P(t)/P$, is proportional to the photoconductance $\Delta S(t)$ [3]:

$$\Delta P(t)/P = A\ \Delta S(t) = A\ (\Delta n(t)\mu_n e + \Delta p(t)\ \mu_p e) \qquad (1)$$

where A is a proportionality constant, depending on dark conductivity, thickness etc., and $\Delta n(t)$ ($\Delta p(t)$) is the excess number in cm^{-2} and μ_n (μ_p) is the mobility of electrons (holes). TRMC signals are displayed in arbitrary units (a.u.).

TRMC signals were excited by 10ns (FWHM) pulses at 1064nm, leading to an approximately uniform generation of charge carriers.

Silicon nitride (Si_3N_4) films (70nm thick) were deposited in a commercial parallel-plate plasma deposition reactor (Plasma Technology). These films were deposited on high quality single crystalline p-type (Boron doped) silicon wafers (0.53 mm thick) mostly on both sides. For the sample covered at only one side with Si_3N_4 it was controlled by TRMC measurements induced by 532nm light at the uncovered face of the wafer that this face can be considered as an infinite sink for excess charge carriers [3]. Measurements of the conductance of the samples before and after the deposition of Si_3N_4 by microwave reflection measurements [3] lead to essentially the same results as reported previously: a conductance increase $2x10^{-4}$ Ω^{-1} is observed after deposition of a Si_3N_4 film at one Si surface [2].

TRMC measurements of several pSi wafers with different resistivities yield essentially the same results:
The maximum TRMC signal height (the TRMC amplitude) is proportional to the excitation density in the range covered. A fast initial decay is followed by a slower decay, where the signal shape does not change in the low excitation density range (lower than $3x10^{-8}$ Jcm^{-2}) but the initial decay becomes considerably slower at high excitation densities. The shape of the TRMC signal does not even depend on the resistivity of the wafer in the low excitation density as it can be seen in Fig.1, where as an example the normalized TRMC signals of the three wafers are displayed for excitation by 1064nm light (30nJcm^{-2}):

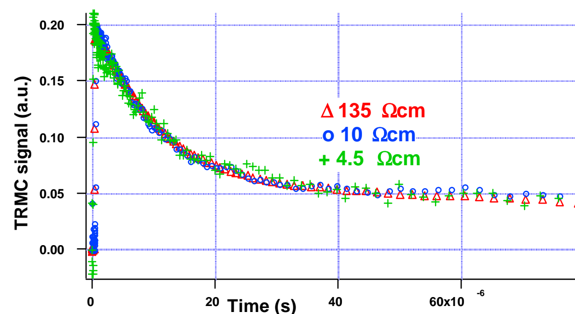

Fig. 1: Normalized TRMC transients induced by 1064 nm light pulses (excitation density 30 nJcm^{-2}) in 3 pSi wafers (0.53 mm) with resistivities 140 Ωcm, 10 Ωcm and 4.5 Ωcm (as indicated in the figure) covered at both sides with Si_3N_4 films in a linear representation

It can be concluded from the experiments that the decay behaviour of the TRMC signal (cf. Fig.1) cannot be due to some volume decay channel but must be due to a process at the Si/Si_3N_4 interface. Furthermore, this decay channel saturates at higher excitation densities .

Further evidence for the attribution of the decay to a junction process comes from experiments on two samples of the same wafer, where one is coated by Si_3N_4 films at both faces and the other one is covered only at one side by a Si_3N_4 film, whereas the other side can be considered as an in infinite sink for excess charge carriers. The shape of the TRMC signal is approximately the same but the slower decaying part of the signal is clearly larger in the sample covered at both sides. Obviously, surface recombination at the uncoated surface competes with the junction process.

Only one process can be related to the initial decay process: the decrease of the minority carrier (electron) mobility in shifting position from the bulk to the Si/Si_3N_4 interface.

The following model seems appropriate:
Excess charge carriers (uniformly generated by 1064nm) diffuse to the junction where electrons are

swept to the interface by the space charge field and holes stay at the edge of the space charge region. The contribution of the holes to the TRMC signal does not change but the contribution of electrons decreases drastically due to the decrease of their mobility. Also a recombination process in the space charge region must be taken into account to explain the long time slower decay. This yields three parameters for the description of excess charge carrier kinetics:

- A rate parameter k_{tr} describing the transport of the generated excess charge carriers to the space charge region.
- The reduced electron mobility μ_n* at the surface.
- The rate parameter k_{rec} describing recombination in the space charge region.

It seems sound to assume that excess charge carrier pairs arriving at the edge of the space charge region are instantaneously separated as long as the space charge field is still considerable. This is evidently only valid at low excitation densities. Then the transport of the excess charge carriers to the space charge regions will be diffusion controlled and k_{tr} is given by [3]:

$$k_{tr} = \frac{D_{amb}\pi^2}{l^2} \qquad (2)$$

where D_{amb} is the ambipolar diffusion constant, given in the low injection range by the minority (electron) diffusion constant. In principle Eq. 2 is not instantaneously valid as first the principal mode must be established [3]. However, application of Eq. 2 in the comparable case of Si wafers with abrased surfaces has learned that a few microseconds after excitation the decay is described by Eq.2 for 1064nm excitation. As a further simplification it will be assumed that the recombination process characterized by k_{rec} is exponential. Under these conditions $\Delta S(t)$ is described by a two exponential equation with only two varying parameters μ_n* and k_{rec}, whereas k_{tr} is given by Eq. 2 and μ_n and μ_p are known.

All experimental data could be fitted within the experimental accuracy by the two exponential equation in the low excitation density range. As an example, experimental data and the best fits are shown for a 400Ωcm pSi wafer (l= 0.53 mm) at both sides covered by a Si_3N_4 film in Fig.2. It can be seen that up to a limiting number of excess carriers $\Delta n_0^{lim}=1\times10^{11}$ cm^{-2} the experimental signals are satisfactorily described by the simple two exponential model.

In Table I the values of k_{rec} and μ_n* found by fitting the experimental data are displayed. The values are obtained by averaging the values obtained for all excitation densities up to a number of generated excess charge carriers Δn_0^{lim} (in cm^{-2}), corresponding to the highest excitation density yielding TRMC signals agreeing with the model. μ_n* is independent of the excitation density, but for k_{rec} the results of some samples suggest a weak increase with Δn_0 . It must be noted that the error in the parameters is relatively large, in particular because the experimental data is rather sensitive to combinations of k_{rec} and μ_n*

Particularly convincing is the agreement between the parameters found for a wafer covered at one side and at two sides with Si_3N_4: within the accuracy of the measurements the same values for k_{rec} and μ_n* are found.

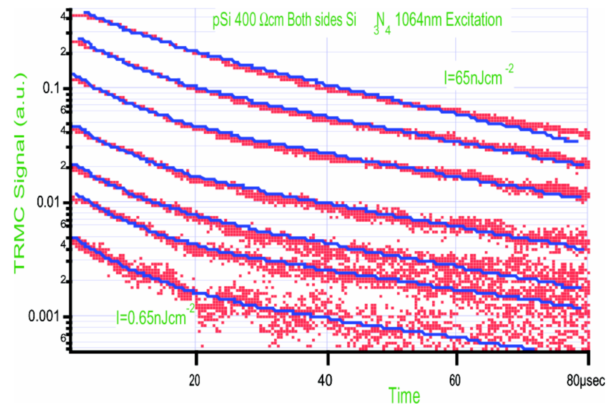

Fig. 2: TRMC transients induced by 1064 nm light pulses (excitation densities from 0.65 - 65 nJcm^{-2}) in a pSi wafer (400 Ωcm, 0.53 mm) covered at both sides with Si_3N_4 films in a semi-logarithmic representation. The (blue) lines drawn represent the best fits of the experimental data to the two exponential model with parameters given in Table I.

Resistivity (Ωcm)	Coa-ted	Δn_0^{lim} (cm^{-2})	μ_n* ($cm^2V^{-1}s^{-1}$)	k_{rec} (s-1)
400	both sides	1×10^{11}	230	2×10^4
400	one side	1×10^{11}	280	2×10^4
140	both sides	1×10^{11}	230	1×10^4
10	both sides	4×10^{11}	200	8×10^3
4.5	both sides	8×10^{11}	200	1×10^4

Table I: The parameters obtained for the best fit of the experimental data to the two exponential model for five samples.

This points to the adequacy of the model for the description of the experimental data. For all samples a value for μ_n* between 200-300 $cm^2V^{-1}s^{-1}$ is found. This indicates that μ_n* can be considered as constant within the accuracy of the experiments. The value for μ_n* agrees satisfactorily with the value μ_n* = 250(-+20%) $cm^2V^{-1}s^{-1}$determined by different measurements [2]. The parameter k_{rec} depends on the deposition conditions and the wafer pretreatment.

The present work shows that excess charge carriers in the space charge region detected by photovoltage measurements are also accessible to (contactless) transient photoconductivity measurements, although with another weight factor

References

[1] M. Kunst, O. Abdallah and F. Wünsch, Thin Solid Films 383, 61 (2001).
[2] J.R. Elmiger and M. Kunst, Appl. Phys. Lett. 69, 517 (1996).
[3] C. Swiatkowski, A. Sanders, K.-D. Buhre and M. Kunst, J. Appl. Phys. 78, 7741 (1995).

S. von Aichberger, G. Citarella, F. Wünsch, M. Kunst

Growth monitoring of reactively sputtered MoS_x and WS_x thin films

The aim of this project is to prepare van-der-Waals-layer type semiconductors MX_2 (M = Mo, W; X = S, Se) which have been proposed as absorber materials for thin film solar cells [1]. Studies have shown that the texture of thin films of these materials is an important factor for their photoactivity (e.g. [2]). The (001) texture, where the van-der-Waals planes are parallel to the substrate surface, is favoured for the application in solar cells because such films have less surface states which can act as charge carrier recombination centres. Since reactive magnetron sputtering from metallic targets in mixtures of argon and a reactive gas (e.g. O_2, H_2, H_2S) is a well established technique for thin film deposition of oxides and sulfides we investigated this method for the deposition of MoS_x and WS_x films. In order to understand the growth mechanisms *in situ* experiments with energy dispersive x-ray diffraction (EDXRD) during the sputtering process were performed at the synchrotron radiation source HASYLAB at DESY, Hamburg.

Analysing the stoichiometry of the films using elastic recoil detection analysis (ERDA) and Rutherford backscattering (RBS) revealed sulphur-to-metal ratios of $x \leq 2.3$, dependent on the amount of H_2S in the H_2S / Ar sputtering gas mixture. Stoichiometric MS_2 is however only formed at substrate temperatures below 200°C, at which the films are practically x-ray amorphous. It was possible to prepare well crystallised films at substrate temperatures of 450°C and above with a suphur/metal ratio of approximately x = 1.7 - 1.8.

In situ-energy dispersive x-ray diffraction (EDXRD)

The setup of the experiment is shown in fig. 1a. At a fixed diffraction angle θ *in situ*-EDXRD spectra were measured by a high purity Ge detector with a time resolution of 20 – 30 s. Fig. 1b depicts a series of spectra which were collected during the deposition of a highly (001) textured WS_x thin film. From the spectra series structural properties of the films were obtained in dependence on the deposition parameters H_2S partial pressure, sputtering power, sputtering pressure ($5 - 90{\cdot}10^{-3}$ mbar), substrate temperature (190 - 620°C) and film thickness. Low deposition rates led to the formation of a strong (001) texture, in which the van-der-Waals planes were parallel to the substrate, which is a prerequisite for high photoactivity of MS_x films ($c_\perp$ orientation of the crystallites). In fig. 2 this is demonstrated for eight experiments where MoS_x films were deposited at increasing sputtering pressure, i.e. decreasing deposition rate. In the diagram the (002) diffraction peak area of the hexagonal MoS_2 phase is plotted against the atomic areal density of the deposited Mo, which represents a normalized film thickness and was calculated from the peak area of the MoK_α fluorescence line. The appearence of the fluorescence lines is due to the use of polychromatic ("white") x-rays and is one advantage of the EDXRD method because it allows a film thickness monitoring additionally to the obtained diffraction pattern. The peak area of the (002) reflection shows a characteristic behaviour during the deposition. A steep increase is followed by a saturation effect. The saturation value of the peak area depends on the sputtering pressure. With increasing pressure this value also increases, indicating that an increasing volume of coherently scattering crystallites, which have their c-axes perpendicular to the substrate ($c_\perp$), is obtained with decreasing deposition rates.

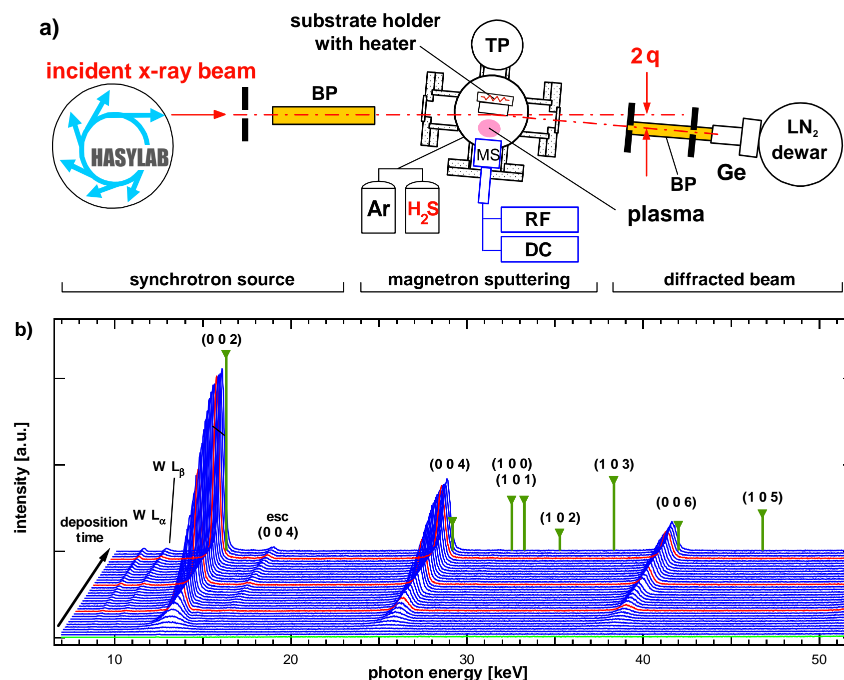

Fig. 1: a) Setup of in situ sputtering chamber for EDXRD experiments at HASYLAB (BP: He-filled beam pipe; TP: turbo pump; MS: magnetron sputtering source; RF, DC: power supplies for the magnetron; Ge: high-purity germanium detector. b) Series of in situ-EDXRD spectra during magnetron sputtering of a WS_x thin film. The green bars with the triangles mark the positions and the intensities of the powder diffraction spectrum of 2H-WS_2 (JCPDS 8-237), esc is an escape peak due to the detection system. Deposition conditions: RF (27.12 MHz) sputtering power 50 W; T_{sub} = 450°C; p_{total} = 0.02 mbar; gas flow ratio F_{H2S} / (F_{H2S}+ F_{Ar}) = 0.75; total deposition time 16 min; diffraction angle θ = 4.474°.

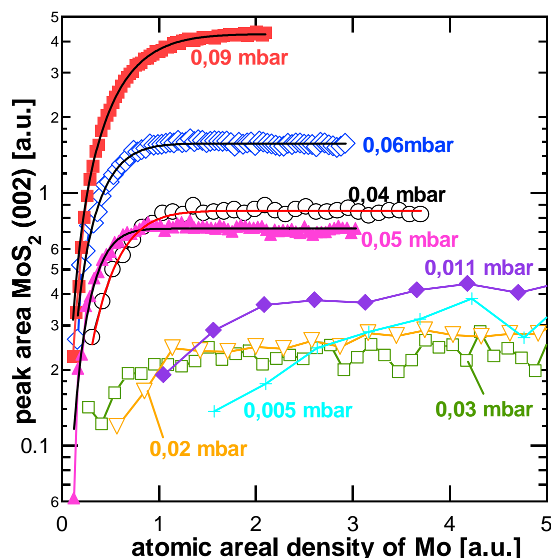

Fig. 2: Development of the peak area of the (002) EDXRD signal during reactive sputtering of MoS_x thin films on oxidized silicon substrates. Eight depositions with varying sputtering pressure are shown. The normalized film thickness is given as atomic areal density of the deposited Mo and was calculated from the MoK_α fluorescence line. Deposition conditions: DC sputtering power 50 W; substrate temperature 450°C; gas flow ratio F_{H2S} / (F_{H2S}+ F_{Ar}) = 0.75; floating substrate potential.

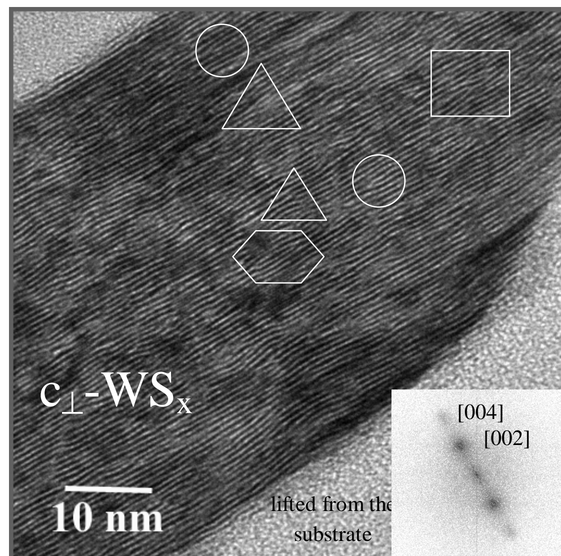

Fig. 3: Cross-sectional TEM picture of a reactively sputtered WS_x thin film on an oxidized silicon substrate. Each black line represents one S-W-S stack, several stacking faults can be observed (marked). The inset is a Fourier transformation of the micrograph showing the diffraction spots of the (002) and (004) lattice planes. Deposition conditions: See fig. 2, substrate temperature 620°C; total sputtering pressure $4{\cdot}10^{-2}$ mbar.

At high deposition rates, the initial (001) preferential orientation of the crystallites turns into a (100) texture. It is proposed that the texture cross-over can be interpreted on the basis of the model of competing contributions of surface energy and microstrain energy to the total energy of the crystallites. The saturation of the (002) peak area shows that the texture crossover is irreversible what can be explained by different growth velocities in the different crystallite directions. Once the (100) orientation occurs it will dominate the subsequent film growth because the crystallites grow 60 - 500 times faster in this direction than in the [001] direction. This value was obtained as approximation by comparing the size of single crystals of these materials in both directions.

Lattice strain and stacking faults

The development of the lattice strain ε of the c-axis relative to the lattice parameter of the powder material could be derived during sputtering from the energetic position of the (002) diffraction peak. It was observed from SEM and TEM images that the (001)-oriented basal layer had a thickness of about 20 nm to a maximum of 100 nm. The strain ε of the c-axis of the unit cell of MoS_2 and WS_2 exhibited a characteristic evolution with increasing film thickness which was proved not to result from mechanical stress in the films. A steep increase in the strain up to a maximum value was observed at the beginning of the deposition followed by a relaxation towards a slightly smaller saturation value. The maximum value of ε was up to 4% depending on the deposition rate [3].

It is assumed that crystal defects such as dislocations, self intercalated metal atoms or by analogy to graphite, turbostratic growth, i.e. a random stacking deviation from the perfectly parallel stacking order of the 2H or 3R polytypes, are responsible for the c lattice strain and grain sizes below 70 nm. This is plausible because of the weak bonds between the S-M-S stacks. The very small grains can be explained by a high defect density, which was confirmed by high resolution cross-sectional TEM analysis of the sputtered films. Fig. 3 shows a detail of a WS_x film in which different stacking faults can be identified. From the micrographs dislocation densities of up to $3{\cdot}10^{12}$ cm^{-2} were estimated. In combination with the metal surplus of many films in comparison to stoichiometric MS_2 the strain of the crystallographic unit cell can also be explained by the intercalation of additional metal atoms between the van-der-Waals planes.

Further *in situ*-EDXRD experiments during reactive sputtering of MoS_x and WS_x thin films are planned to find out wether the variation of the plasma excitation mode (DC and/or RF) and the radio frequency can shift the texture further towards the (001) orientation.

References

[1] H. Tributsch, Z. Naturforsch. 32a, 972 (1977).
[2] E. A. Ponomarev, R. Tenne, A. Katty and C. Levy-Clement, Sol. Energ. Mat. Sol. C. 52, 125 (1998).
[3] V. Weiß, R. Mientus, K. Ellmer, Mat. Res. Soc. Symp. Proc. 721, 131 (2002).

V. Weiß, R. Mientus (Optotransmitter-Umwelt-schutz-Technologie e.V.), U. Bloeck, K. Ellmer